

Review

# Aqueous Zinc–Chalcogen Batteries: Emerging Conversion-Type Energy Storage Systems

Long Zhang <sup>1,\*</sup> and Yongchang Liu <sup>2,\*</sup> 

<sup>1</sup> School of Materials Science and Engineering, University of Science and Technology Beijing, Beijing 100083, China

<sup>2</sup> Beijing Advanced Innovation Center for Materials Genome Engineering, Institute for Advanced Materials and Technology, State Key Laboratory for Advanced Metals and Materials, University of Science and Technology Beijing, Beijing 100083, China

\* Correspondence: zhanglong@ustb.edu.cn (L.Z.); liuyc@ustb.edu.cn (Y.L.)

**Abstract:** Aqueous zinc (Zn) metal batteries are considered competitive candidates for next-generation energy storage, attributed to the abundance, low redox potential, and high theoretical capacity of Zn. However, conventional cathode materials are mainly based on ion-insertion electrochemistry, which can only deliver limited capacity. The conversion-type aqueous zinc–chalcogen batteries (AZCBs) have received widespread attention because they combine the advantages of chalcogen cathodes (S, Se, and Te) and Zn anodes to significantly enhance their capacity. Research on AZCBs has increased continuously; however, it is still in its infancy because the selection and regulation of cathode material systems are not comprehensive and systematic, and the investigation of the mechanisms is not thorough. Herein, we present a detailed overview explaining the recent progress of AZCBs, providing comprehensive guidelines for further research. First, research based on S cathodes, which is the most studied system among AZCBs, is summarized. Second, research based on Se and Te cathodes is described. Research on these different systems is mainly focused on electrolyte modification and cathode optimization. In each section, various strategies are introduced, and the working mechanisms are also discussed. Finally, the challenges and prospects for the development of AZCBs are presented.

**Keywords:** aqueous zinc–chalcogen batteries; aqueous zinc metal batteries; sulfur cathodes; selenium cathodes; tellurium cathodes; electrolyte modifications; cathode optimizations; working mechanisms



**Citation:** Zhang, L.; Liu, Y. Aqueous Zinc–Chalcogen Batteries: Emerging Conversion-Type Energy Storage Systems. *Batteries* **2023**, *9*, 62. <https://doi.org/10.3390/batteries9010062>

Academic Editors: Junnan Hao and King Jet Tseng

Received: 17 November 2022

Revised: 27 December 2022

Accepted: 11 January 2023

Published: 16 January 2023



**Copyright:** © 2023 by the authors. Licensee MDPI, Basel, Switzerland. This article is an open access article distributed under the terms and conditions of the Creative Commons Attribution (CC BY) license (<https://creativecommons.org/licenses/by/4.0/>).

## 1. Introduction

Over the past few decades, the rapid growth of the smart device, electric vehicle, and power grid market has substantially increased the demand for lithium-ion batteries (LIBs) [1–5]. However, developing next-generation secondary batteries has become increasingly urgent because of the safety concerns associated with organic electrolytes, low capacity (372 mAh g<sup>−1</sup> for graphite anodes), and high cost of LIBs, along with potential geopolitical issues related to lithium mineral resources [6–10].

Alkali metal–chalcogen batteries (AMCBs, where AM = lithium (Li), sodium (Na), and potassium (K); C = sulfur (S), selenium (Se), and tellurium (Te)) have attracted considerable attention from researchers owing to the low cost, environment friendliness, and high theoretical specific capacities of chalcogen cathodes (S: 1675 mAh g<sup>−1</sup> or 3416 mAh cm<sup>−3</sup>; Se: 675 mAh g<sup>−1</sup> or 3246 mAh cm<sup>−3</sup>; Te: 419 mAh g<sup>−1</sup> or 2621 mAh cm<sup>−3</sup>) [11–15], as well as the high theoretical specific capacities of alkali metal anodes (Li: 3860 mAh g<sup>−1</sup>, Na: 1166 mAh g<sup>−1</sup>, K: 687 mAh g<sup>−1</sup>) [16–18]. In contrast to the ion-insertion electrochemistry of LIBs, AMCBs are based on reversible redox reactions between chalcogen elements and metal ions to achieve high specific capacity (Figure 1a–c) [19–24]. However, their complex multistep, multielectron reaction mechanism, along with the generation of a series of electrolyte-soluble intermediate products (polysulfides, polyselenides, and polytellurides)

on the cathode side, triggers the notorious shuttle effect, resulting in capacity decay, low rate capability, and low Coulombic efficiency (CE) [25–30]. On the anode side, severe dendrite growth caused by inhomogeneous deposition of metal ions may lead to short circuits and thermal runaway [31–34]. Moreover, safety hazards remain because of the toxicity and flammability of organic electrolytes.

Aqueous rechargeable batteries are safer than energy storage devices using organic electrolytes because they employ water-based electrolytes that are flame-retardant, non-toxic, inexpensive, and highly ion-conductive [35–39]. Therefore, aqueous batteries have greater application potential in wearable electronics and large-scale energy storage devices owing to the high safety requirements of these devices [40–42]. Among aqueous batteries, aqueous Zn metal batteries (AZMBs) have become promising candidates, attributed to the natural abundance of Zn metal, its low redox potential ( $-0.762$  V vs. standard hydrogen electrode), and high theoretical capacity ( $820$  mAh  $g^{-1}$  or  $5855$  mAh  $cm^{-3}$ ) [43–50]. However, typical cathode materials for AZMBs, such as Mn-based oxides, V-based oxides, Mo-based materials, organic compounds, and Prussian blue analogues, are mainly based on ion-insertion electrochemistry, delivering only limited capacities generally less than  $400$  mAh  $g^{-1}$  (Figure 1d) [51–61]. Owing to the lack of compatible high-capacity cathodes, the performance of AZMBs is not fully realized, especially considering the high capacity of Zn anodes. From this perspective, cathode materials based on redox conversion mechanisms offer greater prospects for realizing AZMBs with high capacity and high energy density.

Aqueous zinc–chalcogen batteries (AZCBs) are new types of water-based energy storage systems that have recently attracted research attention because they combine the advantages of chalcogen cathode materials (S, Se, and Te) and AZMBs to significantly improve their capacity and energy density. The significant increase in the capacity of AZCBs depends on redox conversion mechanisms. For example, aqueous Zn–S batteries (AZSBs) are two-electron reaction systems based on the reversible reaction  $S + Zn^{2+} + 2e^{-} \leftrightarrow ZnS$  (Figure 1e); their capacity can exceed  $1000$  mAh  $g^{-1}$ , which is more than twice that of ion-insertion-based systems (Figure 1d) [61–64]. Aqueous Zn–Se batteries (AZSeBs) and Zn–Te batteries (AZTeBs) also follow similar reaction mechanisms ( $Se \leftrightarrow ZnSe$ ;  $Te \leftrightarrow ZnTe_2 \leftrightarrow ZnTe$ ) [65,66], leading to improved electrochemical performance (Figure 1f,g). It is worth noting that all AZCBs are based on one- or two-step solid–solid conversion reaction mechanisms, in which the charge/discharge products in aqueous electrolytes are insoluble, thus eliminating the shuttle effect caused by soluble intermediates in organic electrolytes; this offers significant advantages for improving electrochemical properties. Therefore, introducing chalcogen cathode materials into AZMBs is an effective strategy to improve the electrochemical performance of aqueous batteries, leading to broad application prospects.

Although research on AZCBs has increased continuously, it is still in the initial stage because the selection and regulation of cathode material systems are not comprehensive and systematic, and the exploration of working mechanisms is not thorough. Therefore, it is extremely critical to understand existing research, summarize the current status of AZCBs, provide suggestions and possible solutions for overcoming the challenges associated with AZCBs, and determine the future development prospects of AZCBs to provide comprehensive guidelines for researchers and promote the development of AZCBs. Herein, for the first time, we provide a comprehensive overview of the research on AZCBs to achieve the above goals (Figure 2). First, research on AZSBs based on S cathodes, which are the most studied systems among AZCBs, is summarized. Second, research on AZSeBs and AZTeBs based on Se and Te cathodes is described. Research on these different systems is centered on electrolyte modification and cathode optimization. In each section, various strategies are introduced, and the working mechanisms are explained in detail. Finally, the challenges and prospects for the development of AZCBs are presented.

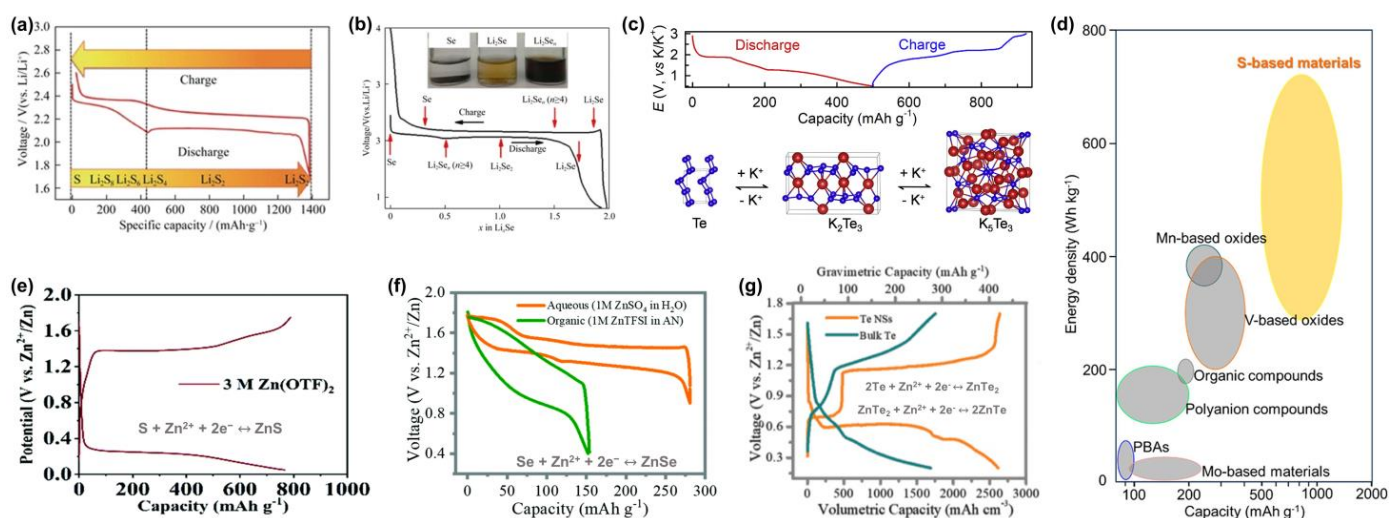


**Figure 1.** Voltage profiles and phase evolutions during charging/discharging of representative AMCBs: (a) Li-S batteries, (b) Li-Se batteries (reproduced with permission from Ref. [22]. Copyright 2017 The Nonferrous Metals Society of China and Springer-Verlag), and (c) K-Te batteries (reproduced with permission from Ref. [23]. Copyright 2020 Elsevier). (d) Comparison of capacities and energy densities of different cathodes in AZMBs (reproduced with permission from Ref. [61]. Copyright 2021, American Chemical Society). Voltage profiles during charging/discharging of representative AZCBs: (e) AZSBs (reproduced with permission from Ref. [64]. Copyright 2022, Royal Society of Chemistry), (f) AZSeBs (reproduced with permission from Ref. [65]. Copyright 2021, Royal Society of Chemistry), and (g) AZTeBs (reproduced with permission from Ref. [66]. Copyright 2020, WILEY-VCH).

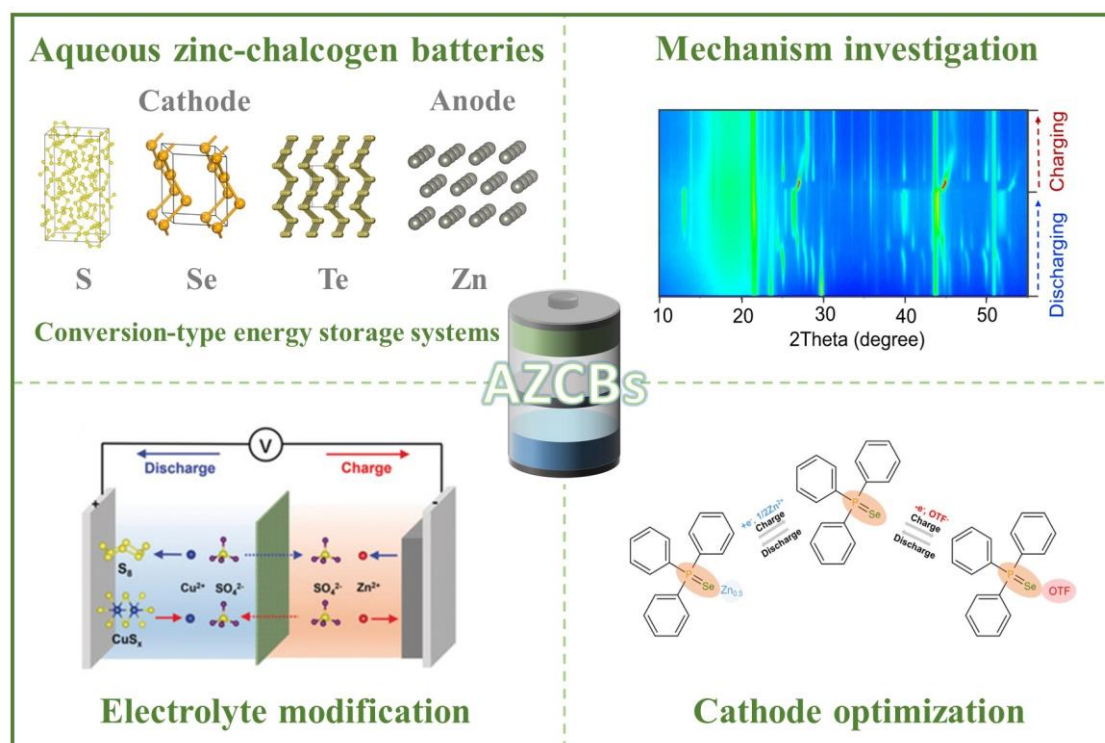


**Figure 2.** A comprehensive review of the research on AZCBs (reproduced with permission from Ref. [66]. Copyright 2020 WILEY-VCH. Reproduced with permission from Ref. [67]. Copyright 2019 WILEY-VCH. Reproduced with permission from Ref. [68]. Copyright 2022 Springer Nature. Reproduced with permission from Ref. [69]. Copyright 2022 Elsevier).

## 2. Aqueous Zn–S Batteries (AZSBs)

Although AZSBs are relatively mature AZCB systems, the following issues need to be solved: (1) The poor electronic conductivity of S ( $5 \times 10^{-28} \text{ S m}^{-1}$ ) and ZnS ( $10^{-9} \text{ S m}^{-1}$ ), and the large volume change (50.3%) during cycling seriously affect the rate performance and cycling stability of AZSBs [61,70–72]. (2) The solid–solid conversion mechanisms of S and ZnS in aqueous electrolytes avoid the shuttle effect but slow the kinetics of the conversion reaction [73]. (3) In aqueous electrolytes, the disproportionation reaction of ZnS occurs during charging to form irreversible  $\text{SO}_4^{2-}$ , leading to the loss of active materials [74]. (4) For Zn metal anodes, corrosion, hydrogen evolution, and uncontrolled dendrite growth are more serious after coupling with the conversion-type chalcogen cathodes, leading to further deteriorated electrochemical performance [75–79]. To address these challenging problems, several efforts have been made to rationally optimize AZSBs, mainly focusing on electrolyte modification and cathode optimization. In this section, research on improving the performance of AZSBs is described in detail, along with comprehensive explanations of their working mechanisms.

### 2.1. Electrolyte Modification for AZSBs

#### 2.1.1. Choice of Solute, Concentration, and Solvent for AZSBs

Ji et al. first evaluated the electrochemical properties of disposable AZSBs in different electrolytes with S as the cathode and Zn foil as the anode [80]. The S cathode was fabricated by infiltrating elemental S into Ketjen Black (KB) to enhance conductivity. They found that in different electrolytes (1 M  $\text{ZnCl}_2$ ,  $\text{Zn}(\text{CH}_3\text{COO})_2$  ( $\text{Zn}(\text{AC})_2$ ),  $\text{Zn}(\text{CF}_3\text{SO}_3)_2$  ( $\text{Zn}(\text{OTF})_2$ ), and  $\text{ZnSO}_4$ ), the open circuit voltages of AZSBs were generally around 1 V, whereas the discharge voltages and specific capacities varied dramatically (Figure 3a). The AZSBs delivered the highest discharge voltage of approximately 0.7 V in 1 M  $\text{ZnCl}_2$  electrolyte with a specific capacity of  $1668 \text{ mAh g}^{-1}$  at  $50 \text{ mA g}^{-1}$ , corresponding to a high energy density of  $1083.3 \text{ Wh kg}^{-1}$ . The difference in the discharge voltage could be attributed to the different interfacial charge transfer resistance ( $R_{\text{ct}}$ ) values of the S cathode in different electrolytes;  $R_{\text{ct}}$  is the lowest in 1 M  $\text{ZnCl}_2$  (Figure 3b), which is beneficial for improving the reaction kinetics. According to a previous report [81], the dehydration process of  $[\text{ZnCl}(\text{H}_2\text{O})_5]^+$  clusters requires less energy than  $[\text{Zn}(\text{H}_2\text{O})_6]^{2+}$  clusters, thus resulting in a lower  $R_{\text{ct}}$  in  $\text{ZnCl}_2$  than in other electrolytes. Therefore, AZSBs based on the  $\text{ZnCl}_2$  electrolyte exhibited high rate performance and operated under a high mass loading of  $8.3 \text{ mg cm}^{-2}$  for the S cathode, achieving a high areal capacity of  $11.4 \text{ mAh cm}^{-2}$  (Figure 3c). Moreover, AZSBs based on the  $\text{ZnCl}_2$  electrolyte showed high capacity retention (80.1%) even after resting for 21 days, indicating a moderate self-discharge rate that could be beneficial for practical applications.

Further, Li et al. studied the influence of electrolyte concentration on the electrochemical performance of AZSBs [64]. The  $\text{Zn}(\text{OTF})_2$  electrolyte was selected instead of  $\text{Zn}(\text{AC})_2$  and  $\text{ZnSO}_4$  because the larger  $\text{CF}_3\text{SO}_3^-$  anions could decrease the number of  $\text{H}_2\text{O}$  molecules in the solvated shell structure of  $\text{Zn}^{2+}$  and suppress the solvation effect of  $\text{Zn}^{2+}$  [82]. Porous carbon (CMK-3) was chosen as the host material for the S cathode to enhance conductivity. As shown in Figure 3d, the cycling performance of AZSBs in the high-concentration electrolyte (3 M  $\text{Zn}(\text{OTF})_2$ ) was more stable, and the capacity retention rate was much higher than that in the low-concentration electrolytes (15% in 1 M  $\text{Zn}(\text{OTF})_2$ , 23% in 2 M  $\text{Zn}(\text{OTF})_2$ , and 61% in 3 M  $\text{Zn}(\text{OTF})_2$ ). After further investigation, they found that a higher electrolyte concentration could lower the corrosion of Zn metal, thus yielding a more positive Zn corrosion potential and a lower corrosion current (Figure 3e). In addition, as displayed in the linear sweep voltammetry (LSV) curves (Figure 3f), a low linear potential of  $-1.08 \text{ V}$  was obtained in 3 M  $\text{Zn}(\text{OTF})_2$ , suggesting a wider electrochemical window. Therefore, the AZSBs with a high electrolyte concentration (3 M  $\text{Zn}(\text{OTF})_2$ ) could deliver high electrochemical performance.

Huang et al. designed a deep eutectic solvent (DES, Figure 3g) composed of low-cost urea (hydrogen bond donor) and choline chloride (ChCl, hydrogen bond acceptor)

with a stoichiometric ratio of 2:1 to solve the issues such as narrow voltage windows, side reactions, and Zn dendrite growth in aqueous electrolytes [83]. The ChCl/urea DES was colorless and transparent, with good solubility for different Zn salts (such as  $\text{ZnCl}_2$ ,  $\text{Zn}(\text{NO}_3)_2$ ,  $\text{Zn}(\text{Ac})_2$ , and  $\text{ZnSO}_4$ ) (Figure 3h). As displayed in Figure 3i, the overall voltage window for the DES– $\text{ZnCl}_2$  electrolyte was expanded to 4.65 V, which was much wider than that of the aqueous  $\text{ZnSO}_4$  electrolyte, indicating that the side reactions could be effectively suppressed in DES-based electrolytes. Owing to the suppression of side reactions caused by the absence of water, the  $\text{Zn}^{2+}$  solvation structure in DES-based electrolytes was reasonably optimized, leading to dendrite-free Zn stripping/plating behavior over 3900 h (Figure 3j). Based on these advantages, the AZSBs exhibited a high capacity of  $846 \text{ mAh g}^{-1}$  (based on the mass of S) and corresponding energy density of  $259 \text{ Wh kg}^{-1}$  at  $0.5 \text{ A g}^{-1}$  (Figure 3k). More importantly, a decent anti-self-discharge performance from the AZSBs was also realized, with the capacity retention maintained at 94.58% and 68.58% after resting for 72 and 288 h, respectively.

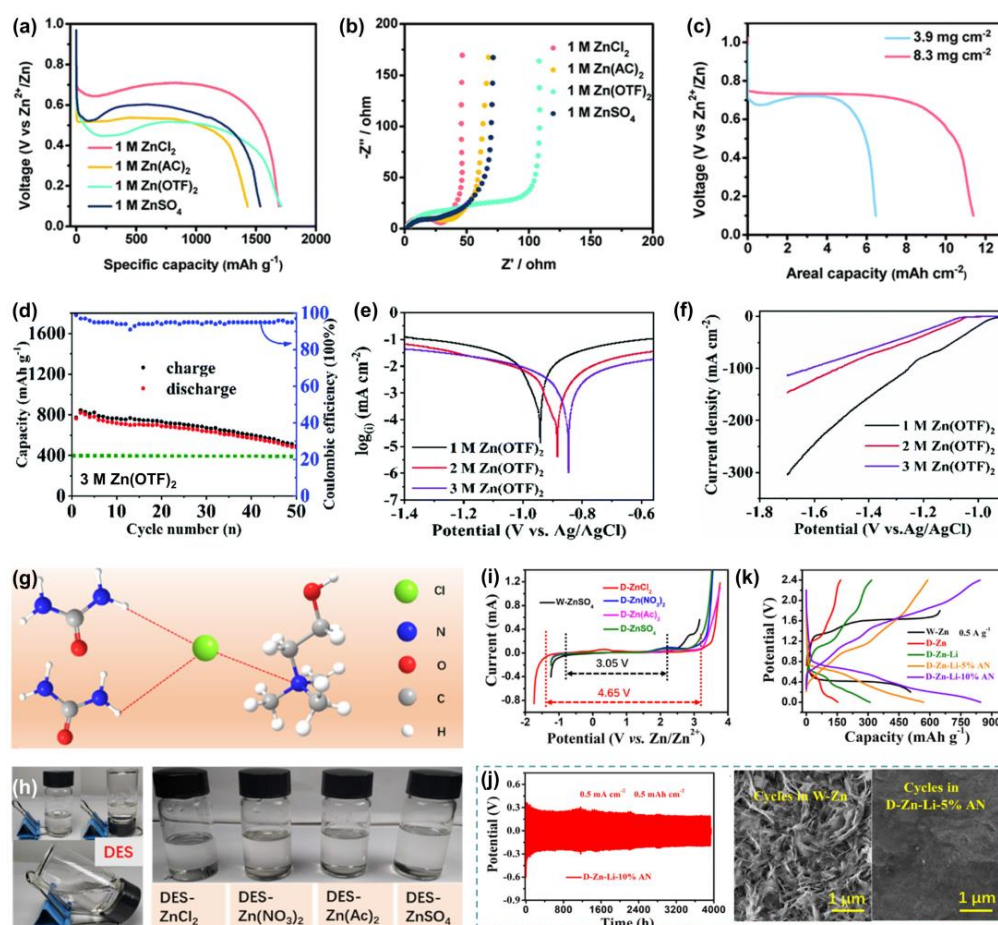


**Figure 3.** (a) Discharge curves and (b) electrochemical impedance spectroscopy (EIS) spectra of AZSBs using different electrolytes; (c) discharge curves with different S mass-loading of AZSBs (reproduced with permission from Ref. [80]. Copyright 2021, Royal Society of Chemistry). (d) Cycling performance of AZSBs at  $200 \text{ mA g}^{-1}$  in  $3 \text{ M Zn}(\text{OTF})_2$  electrolyte, (e) corrosion potentials and (f) LSV curves of Zn anodes in the  $\text{Zn}(\text{OTF})_2$  electrolyte with different concentrations (reproduced with permission from Ref. [64]. Copyright 2022, Royal Society of Chemistry). (g) Illustration of the ChCl/urea DES; (h) different Zn salts dissolved in the DES; (i) electrochemical windows of AZSBs in different electrolytes; (j) cycling test of the Zn symmetrical cell in DES-based electrolyte, and scanning electron microscopy (SEM) images of different Zn anodes; (k) galvanostatic charge–discharge (GCD) curves of AZSBs in different electrolytes (reproduced with permission from Ref. [83]. Copyright 2021, American Chemical Society).

### 2.1.2. Choice of Electrolyte Additive for AZSBs

Adding additives into electrolytes is also an effective strategy to improve the electrochemical properties of AZSBs. The current strategies for the S cathode are mainly divided into two types; one is to improve the redox conversion reversibility of S and ZnS without changing the overall two-electron reaction process, whereas the other is to improve the conversion kinetics and increase the capacity by changing the two-electron reaction to the four-electron reaction. Both strategies are described in detail below.

- Without changing the two-electron reaction process.

In AZSBs, owing to the uneven accumulation of discharge products (ZnS), the conversion of ZnS to S during charging is significantly hindered, leading to decreased conversion reversibility and slow kinetics. To solve this problem, Zhu et al. added PEG-400 to the 1 M Zn(AC)<sub>2</sub> electrolyte for achieving uniform nucleation of ZnS (Figure 4a) [63]. The Raman and <sup>1</sup>H NMR results (Figure 4b,c) revealed that the PEG molecules entered the solvation sheath of Zn<sup>2+</sup> and replaced part of the H<sub>2</sub>O molecules in the primary solvation shell, thereby significantly changing the coordination environment of Zn<sup>2+</sup> and forming a modified solvation structure. Taking advantage of the new solvation structure, small (180 nm) and uniform ZnS products could be formed during discharging, which was conducive to the reversible conversion of ZnS to S with lower polarization. Therefore, the S@carbon nanotubes (CNTs) cathode with this aqueous electrolyte exhibited a low voltage hysteresis of 0.47 V, high specific capacity of 1116 mAh g<sup>-1</sup> at 0.1 A g<sup>-1</sup>, and high rate performance (Figure 4d,e). Ex situ X-ray powder diffraction (XRD) and Raman results (Figure 4f–h) clearly demonstrated excellent reversibility of the conversion reaction from ZnS to S in AZSBs, indicating the effectiveness of PEG-400.

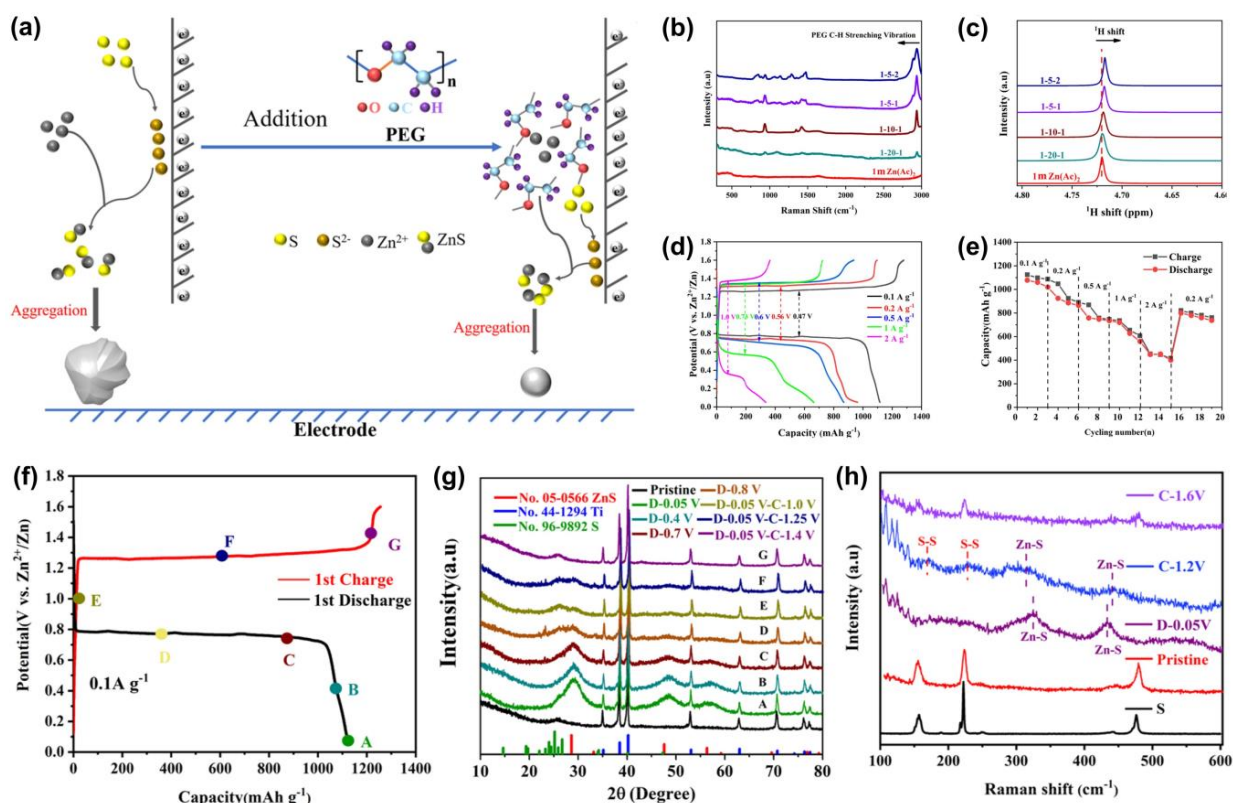


**Figure 4.** (a) Schematic of the effect of PEG additive; (b) Raman spectra and (c) <sup>1</sup>H NMR spectra of different electrolytes; (d) GCD curves and (e) capacity evolution at different current densities; (f) GCD curve at 0.1 A g<sup>-1</sup> and (g) corresponding ex situ XRD patterns; (h) Raman spectra of the S cathode at different charge/discharge states (Reproduced with permission from Ref. [63]. Copyright 2022, Elsevier).

- Changing the two-electron reaction to the four-electron reaction

### 1. Cu-based redox charge carrier

Ji et al. found that the Cu–S redox-ion electrode could deliver a high capacity of 3044 mAh g<sup>-1</sup> (Figure 5a) [67]. Further X-ray absorption near-edge structure (XANES) and ex situ XRD results revealed the reaction mechanism of this system: the S cathode with Cu<sup>2+</sup> as the charge carrier underwent four-electron redox reactions through the conversion sequence of S ↔ CuS ↔ Cu<sub>2</sub>S (Figure 5b,c), thus obtaining a higher specific capacity. The reaction processes are as follows:

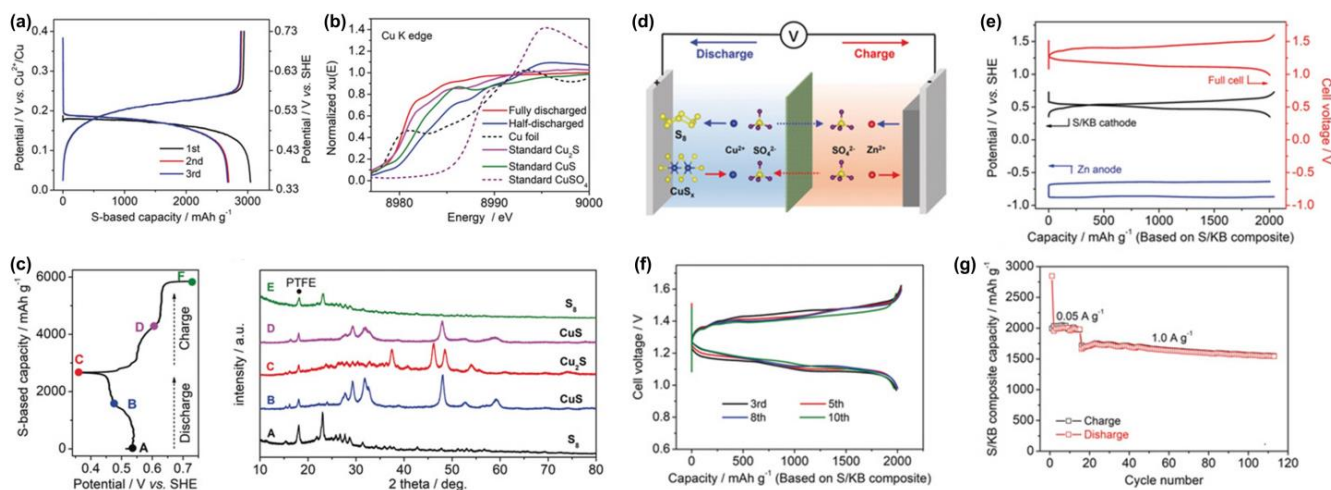


**Figure 5.** (a) GCD curves of the S cathode in a three-electrate cell at 100 mA g<sup>-1</sup>; (b) XANES spectra of the Cu-K edge; (c) GCD curve at 10 mA g<sup>-1</sup> and corresponding ex situ XRD patterns; (d) illustration of the mechanism; (e) GCD curves of the S cathode, Zn anode, and corresponding hybrid cell; (f) GCD curves at 50 mA g<sup>-1</sup> and (g) cycling performance of the hybrid cell (reproduced with permission from Ref. [67]. Copyright 2019, Wiley-VCH).

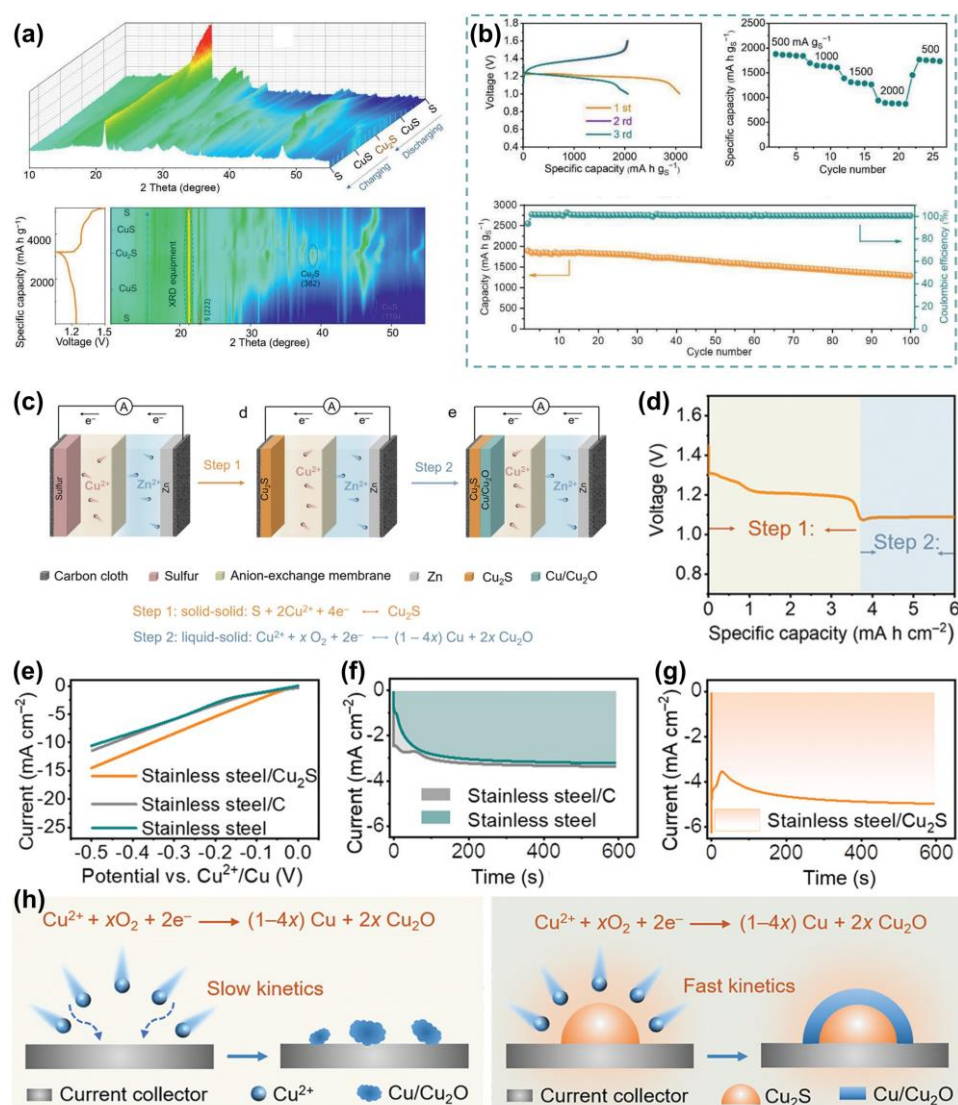
However, the direct use of Cu as an anode in a full battery is of little practical value because of the low discharge voltage plateau of 0.18 V (Figure 5a). To solve this issue, they used an anion exchange membrane as the separator to divide the cell into two parts: one for the Cu–S redox-ion cathode and one for the Zn anode. Thus, the hybrid AZSBs (S, CuSO<sub>4</sub> || ZnSO<sub>4</sub>, Zn) were assembled, and the working mechanism is shown in Figure 5d. During the discharge process, the S cathode generated Cu<sub>2</sub>S through the four-electron transfer process, and the Zn metal was stripped to Zn<sup>2+</sup>; during the charge process, the reaction direction was reversed. The discharge reaction processes are as follows:



Figure 5e illustrated the typical GCD potential profiles of the S cathode and Zn anode, where the Zn anode operated at approximately -0.7 V (vs. standard hydrogen electrode, SHE). As shown in Figure 5f, the hybrid AZSBs delivered a high capacity (~2000 mAh g<sup>-1</sup>) with a decent cell voltage (~1.15 V) and low polarization (~0.3 V). Moreover, the hybrid AZSBs exhibited good cycling stability at both low and high current rates (0.05 A g<sup>-1</sup> and 1.0 A g<sup>-1</sup>, Figure 5g).

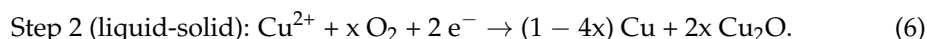
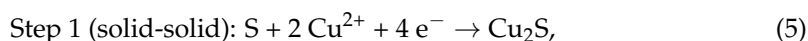
Qu et al. developed flexible aqueous batteries based on the working mechanism of the above hybrid AZSBs with Cu<sup>2+</sup> as the charge carrier [62]. The introduction of the anion

exchange membrane could effectively prevent the cross-diffusion of  $\text{Cu}^{2+}/\text{Zn}^{2+}$  cations between the quasi-solid gelatin/ $\text{CuSO}_4$  catholyte and gelatin/ $\text{ZnSO}_4$  anolyte, thereby inhibiting the spontaneous reaction between  $\text{Cu}^{2+}$  and Zn metal and the accompanying self-discharge behavior. This new type of hybrid system of AZSBs possessed a high theoretical capacity of  $3350 \text{ mAh g}_s^{-1}$  and volumetric energy density of  $3868 \text{ Wh L}^{-1}$ , substantially exceeding the AZSBs that relied on a single carrier. In situ XRD results (Figure 6a) clearly verified the reaction mechanism of the S cathode in hybrid AZSBs; the S cathode first converted to  $\text{CuS}$  and then to  $\text{Cu}_2\text{S}$ , delivering four-electron redox reactions during discharging. As shown in Figure 6b, the flexible hybrid AZSBs exhibited high capacity (initial capacity of  $3084 \text{ mAh g}_s^{-1}$ , reversible capacity of  $2063 \text{ mAh g}_s^{-1}$  at  $100 \text{ mA g}_s^{-1}$ ), high rate performance ( $938 \text{ mAh g}_s^{-1}$  at  $2000 \text{ mA g}_s^{-1}$ ), and long-term cycling performance ( $1442 \text{ mAh g}_s^{-1}$  maintained after 100 cycles at  $500 \text{ mA g}_s^{-1}$ ). Moreover, a single flexible hybrid cell could power an electric fan that kept turning at the same speed even when the cell was severely bent and deformed.



**Figure 6.** (a) In situ XRD patterns and (b) initial three GCD curves, rate and cycling performance of the hybrid AZSBs (reproduced with permission from Ref. [62]. Copyright 2021, Wiley-VCH). (c) Working mechanisms and (d) the typical discharge curve of ACB; (e) LSV curves and (f,g) potentiostatic deposition curves of different current collectors; (h) schematic of  $\text{Cu}/\text{Cu}_2\text{O}$  deposited on the bare current collector and  $\text{Cu}_2\text{S}$ , respectively (reproduced with permission from Ref. [84]. Copyright 2021, Wiley-VCH).

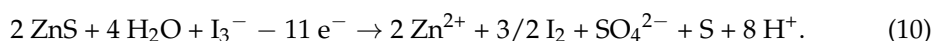
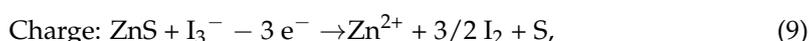
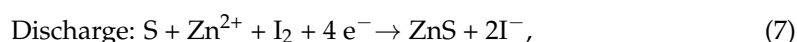
Qu et al. further constructed an aqueous cascade battery (ACB, coupling two sequential electrochemical reactions) based on hybrid AZSB systems with  $\text{Cu}^{2+}$  as the charge carrier [84]. In the first discharge step of the cascade battery, the S cathode generated  $\text{Cu}_2\text{S}$  through the four-electron solid–solid conversion reaction; after the solid S was consumed, the  $\text{Cu}^{2+}$  cations in the catholyte were further reduced into the Cu/ $\text{Cu}_2\text{O}$  composite (solid state), which further supplied energy output in the second discharge step (Figure 6c,d). The generation of  $\text{Cu}_2\text{O}$  was mainly attributed to the dissolved oxygen in electrolyte. The following are the discharge reaction processes:



A series of electrochemical test results (LSV curves and potentiostatic deposition curves, Figure 6e–g) revealed that  $\text{Cu}_2\text{S}$ , the discharge product in the first discharge step, could serve as a catalyst to accelerate the reaction kinetics of the second discharge step in the ACB (Figure 6h). Based on the advantages of such reaction mechanisms, the cascade battery exhibited excellent cycling performance (100 cycles (~2 months) without obvious capacity attenuation) and high areal capacity with high S loading ( $48 \text{ mAh cm}^{-2}$  with  $9.6 \text{ mg cm}^{-2}$ ). Moreover, the quasi-solid-state ACB was further assembled, and it exhibited similar discharge/charge curves even after 1000 bending deformations, cutting a half off, and piercing 100 times, possessing excellent flexibility, high safety, and superior anti-destructive ability.

## 2. I-based redox charge carrier

Jiang et al. reported employing electrolyte additive  $\text{I}_2$  as the charge carrier to improve the electrochemical performance of AZSBs, i.e., adding 0.05 wt%  $\text{I}_2$  into 1 M  $\text{Zn}(\text{AC})_2$  electrolyte (pH = 6.5) [74]. As shown in the GCD curves, the S cathode with  $\text{I}_2$  delivered a high reversible capacity of  $1105 \text{ mAh g}^{-1}$  with a flat discharge voltage of 0.5 V, achieving a high energy density of  $502 \text{ Wh kg}^{-1}$  (Figure 7a,b). In addition, the total cost of the AZSBs could be reduced to  $\$45 \text{ kWh}^{-1}$ , lower than other common energy storage systems, because of the cheap raw materials (Figure 7c). Ex situ XRD, Raman, and X-ray photoelectron spectroscopy (XPS) results (Figure 7d–f) revealed that the S cathode underwent a redox reaction between S and ZnS. However, the characteristic signal of  $\text{SO}_4^{2-}$  was also detected in the charging product (XPS spectra of S 2p), indicating that part of the ZnS was irreversibly oxidized to  $\text{SO}_4^{2-}$  by dissolved  $\text{O}_2$  during charging, resulting in capacity decay. This disproportionation reaction could be suppressed by reducing the surface-exposed S in the cathode and removing the dissolved  $\text{O}_2$  in the electrolyte. As shown in the XPS spectra of I 3d, the intense characteristic signal of I was also detected at the discharge and charge states, besides Zn and S signals. The peaks were ascribed to  $\text{I}^-$  and the ligand of  $\text{I}_3^-$  at the discharge state (0.05 V), whereas the peaks were attributed to  $\text{I}_2$  at the charge state (1.6 V). The change in binding energy for I at the discharge/charge states indicated the redox conversion of the  $\text{I}_2$  additive, in which  $\text{I}_2$  could act as the  $\text{Zn}^{2+}$  carrier and reduce the reaction barrier [85,86]. Thus,  $\text{I}_2$  was first reduced to  $\text{I}^-$  that continued reacting with  $\text{I}_2$  to form  $\text{I}_3^-$  during discharging, and ZnS and  $\text{I}_3^-$  were oxidized simultaneously during charging. The following are the possible cathode reaction processes:



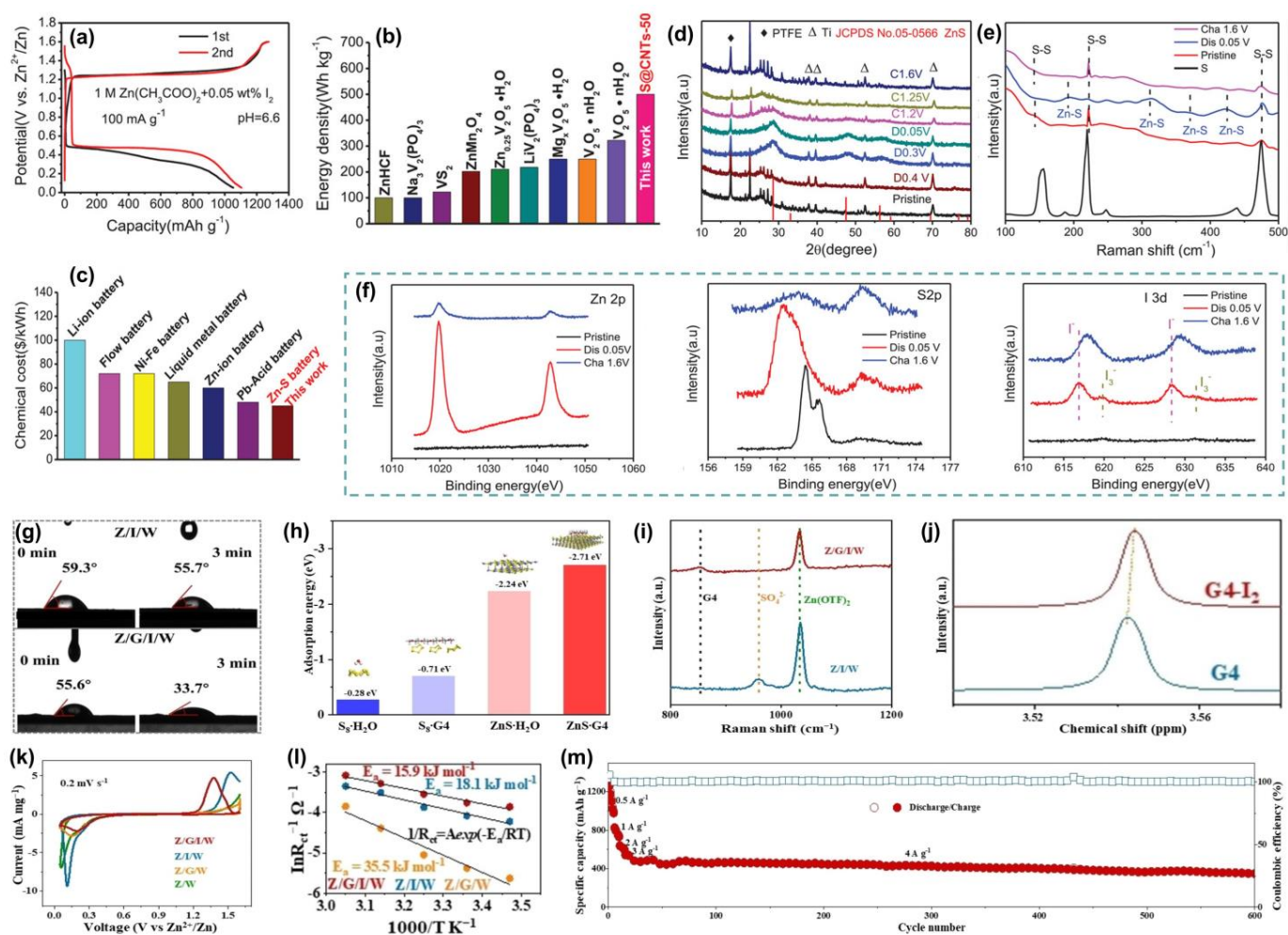
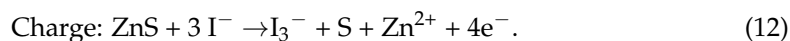
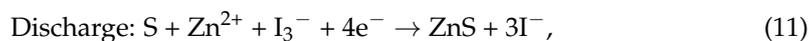


**Figure 7.** (a) GCD curves of the S cathode in 1 M  $\text{Zn}(\text{AC})_2$  with 0.05 wt%  $\text{I}_2$  additive; comparison of (b) energy density and (c) total cost of the AZSBs with other batteries; (d) ex situ XRD patterns and (e) Raman spectra of the S cathode at different states; (f) XPS spectra of Zn 2p, S 2p, and I 3d at different states (reproduced with permission from Ref. [74]. Copyright 2020, Wiley-VCH). (g) Water contact angle test of different electrolytes; (h) adsorption energies of different ligands; (i) Raman spectra of the S cathodes after cycles in different electrolytes; (j)  $^1\text{H}$  NMR spectra of G4 and G4- $\text{I}_2$ ; (k) CV curves of the AZSBs in different electrolytes; (l) activation energies of different electrolytes; (m) cycling performance of the AZSBs using the optimized electrolyte (reproduced with permission from Ref. [73]. Copyright 2022, Wiley-VCH).

The above reaction equations demonstrated good reversibility of the  $\text{I}_2$ – $\text{I}_3^-$  redox couple, indicating that the  $\text{I}_2$  additive could be steadily used as the  $\text{Zn}^{2+}$  carrier. In summary,  $\text{I}_2$  could change the two-electron process of AZSBs into the four-electron process, thereby improving the electrochemical performance.

However, the nonpolar  $\text{I}_2$  additive interacts weakly with the S cathode and accelerates the corrosion of the Zn anode, thus deteriorating the electrochemical performance [87,88]. To solve these issues, Zhu et al. designed a cocktail-optimized electrolyte with  $\text{H}_2\text{O}$  and tetraglyme (G4) as the cosolvent,  $\text{I}_2$  as the additive, and  $\text{Zn}(\text{OTF})_2$  as the Zn salt, in which G4 and  $\text{I}_2$  functioned synergistically to improve the electrode reversibility of AZSBs [73]. The strong affinity of G4 to the S cathode could improve the wettability of the electrolytes and inhibit their access to  $\text{H}_2\text{O}$  (Figure 7g,h), thereby effectively promoting the transport of  $\text{Zn}^{2+}$  ions and suppressing the generation of the disproportioning product ( $\text{SO}_4^{2-}$ ) during the redox conversion of S (Figure 7i). Moreover,  $\text{I}_2$  could be reduced to  $\text{I}_3^-$  by the electron donor ( $-\text{COC}-$ ) of G4 (Figure 7j), which was more effective in catalyzing the

solid–solid redox conversion of the S cathode, resulting in a lower polarization (Figure 7k) and decreased activation energy ( $15.9 \text{ kJ mol}^{-1}$ , Figure 7l). Therefore, the following are the improved reaction processes:



For the anode side, owing to the presence of G4, the partially decomposed  $\text{Zn}(\text{OTf})_2$  triggered by  $\text{I}_3^-$  could form an organic–inorganic solid electrolyte interface (SEI) on the Zn surface during the cycling process, which could prevent side reactions such as corrosion and regulate the diffusion and deposition of  $\text{Zn}^{2+}$  ions, leading to dendrite-free Zn stripping/plating behavior over 1800 h at  $5 \text{ mA cm}^{-2}$  with  $5 \text{ mAh cm}^{-2}$ . Therefore, the AZSBs with the cocktail-optimized electrolyte delivered a high capacity ( $775 \text{ mAh g}^{-1}$  at  $2 \text{ A g}^{-1}$ ), high rate capability, and long cycling life ( $349 \text{ mAh g}^{-1}$  after 600 cycles at  $4 \text{ A g}^{-1}$ , Figure 7m). Furthermore, the pouch cell also exhibited decent electrochemical performance.

## 2.2. Cathode Optimization for AZSBs

To improve the conversion kinetics of AZSBs and track their degradation mechanism, Lu et al. designed an  $\text{Fe}(\text{CN})_6^{4-}$ -doped polyaniline-wrapped S composite cathode (S@Fe-PANi) through in situ interfacial polymerization (Figure 8a) [61]. An iron-based redox pair,  $\text{Fe}^{\text{II}}(\text{CN})_6^{4-}/\text{Fe}^{\text{III}}(\text{CN})_6^{3-}$  redox couple, was introduced in this composite cathode. The iron redox enabled the three-dimensional (3D)  $\text{Zn}^{2+}$  ion to migrate from the inserted  $\text{Zn}_x\text{Fe}^{\text{II}}(\text{CN})_6$  to S, accelerating the sluggish kinetics of the reduction reaction. Moreover, the diffusion of  $\text{Zn}^{2+}$  was realized during the oxidation process of S, which was essential for reducing the oxidation energy barrier of ZnS and thus achieving high-performance S redox chemistry guided by redox catalysis (Figure 8b). The authors later identified the redox couple as  $\text{Zn}_x\text{PANi-ZnFe}^{\text{III}}(\text{CN})_6/\text{Zn}_x\text{PANi-ZnFe}^{\text{II}}(\text{CN})_6$  in the addition/correction for this work because of the strong binding between PANi and  $\text{Fe}(\text{CN})_6^{4-}$  and the fact that the electrode slightly altered the redox potential of  $\text{Fe}^{\text{III/II}}$  [61]. The experimental results indicated that the Fe-based redox couple could reduce the voltage hysteresis, increase the specific capacity, and prolongate the cycling life of AZSBs, which proved that the redox couple was related to accelerating the S redox kinetics. The ex situ XRD patterns and XPS spectra (Figure 8c,d) of S@Fe-PANi cathodes showed that the characteristic peaks of ZnS followed the same trend of appearing, increasing, attenuating, and disappearing during the discharge/charge process, verifying the reversibility of S to ZnS. Such reversible reactions were attributed to the fast S redox kinetics promoted by the Fe-based redox couple.

Zhi et al. reported a reliable and reversible AZSB system activated by a “liquid film” [89]. In this system, the poly( $\text{Li}_2\text{S}_6$ -random-(1,3-diisopropenylbenzene)) copolymer (poly( $\text{Li}_2\text{S}_6$ -r-DIB), PLSD) was introduced, where  $\text{Li}_2\text{S}_6$  (lithium polysulfide) was used as the cathode of AZSBs in 1 M zinc bis(trifluoromethylsulfonyl)imide ( $\text{Zn}(\text{TFSI})_2$ ) electrolyte, and DIB acted as an anchor for polysulfides, inhibiting the shuttle effect through strong covalent interactions. To better protect the cathode, the surface of the cathode was coated with a so-called liquid film, containing 4-(3-butyl-1-imidazolium)-1-butananesulfoni ionic liquid encapsulated within the poly(3,4-ethylenedioxythiophene):poly(styrenesulfonate) (PEDOT:PSS) 3D scaffold. In other words, the introduced PEDOT:PSS skeleton held ionic liquid (IL) in a form of liquid film (LF) on the cathode surface. The advantages of the LF are described as follows (Figure 8e): the  $\text{CF}_3\text{SO}_3^-$  anions in IL operated as transfer channels of  $\text{Zn}^{2+}$ , whereas the TFSI<sup>−</sup> anions in the electrolyte were blocked by these channels because of their large size; PEDOT:PSS formed a 3D network that could immobilize IL ions in the LF-PLSD cathode, substantially enhancing the structural stability. On the contrary, for the IL-PLSD cathode without LF coating, with  $\text{Zn}^{2+}$  ions entering and leaving through the channels, the IL coating on the PLSD gradually diffused into the electrolyte, resulting in a continuous weakening and eventually disappearance of the channel effect. As displayed in Figure 8f, the  $\text{S}_6^{2-}$  anions were mainly reduced to  $\text{S}^{2-}$  by Zn during the discharge process,

and these short-chain products were oxidized to generate long-chain  $Zn_xLi_yS_{3-6}$  during the charge process. Based on such a working mechanism and the protection offered by the LF coating, the Zn/LF-PLSD full cell delivered an excellent capacity of  $1148 \text{ mAh g}^{-1}$  at  $0.3 \text{ A g}^{-1}$  (Figure 8g). After optimization by the highly concentrated salt electrolyte, the Zn/LF-PLSD cell exhibited a high rate performance (Figure 8h) and an extended lifetime. The quasi-solid Zn/LF-PLSD pouch cell was further assembled based on the hydrogel electrolyte (Figure 8i) and exhibited stable cycling life ( $247 \text{ mAh g}^{-1}$  maintained at  $1 \text{ A g}^{-1}$  after 900 cycles).

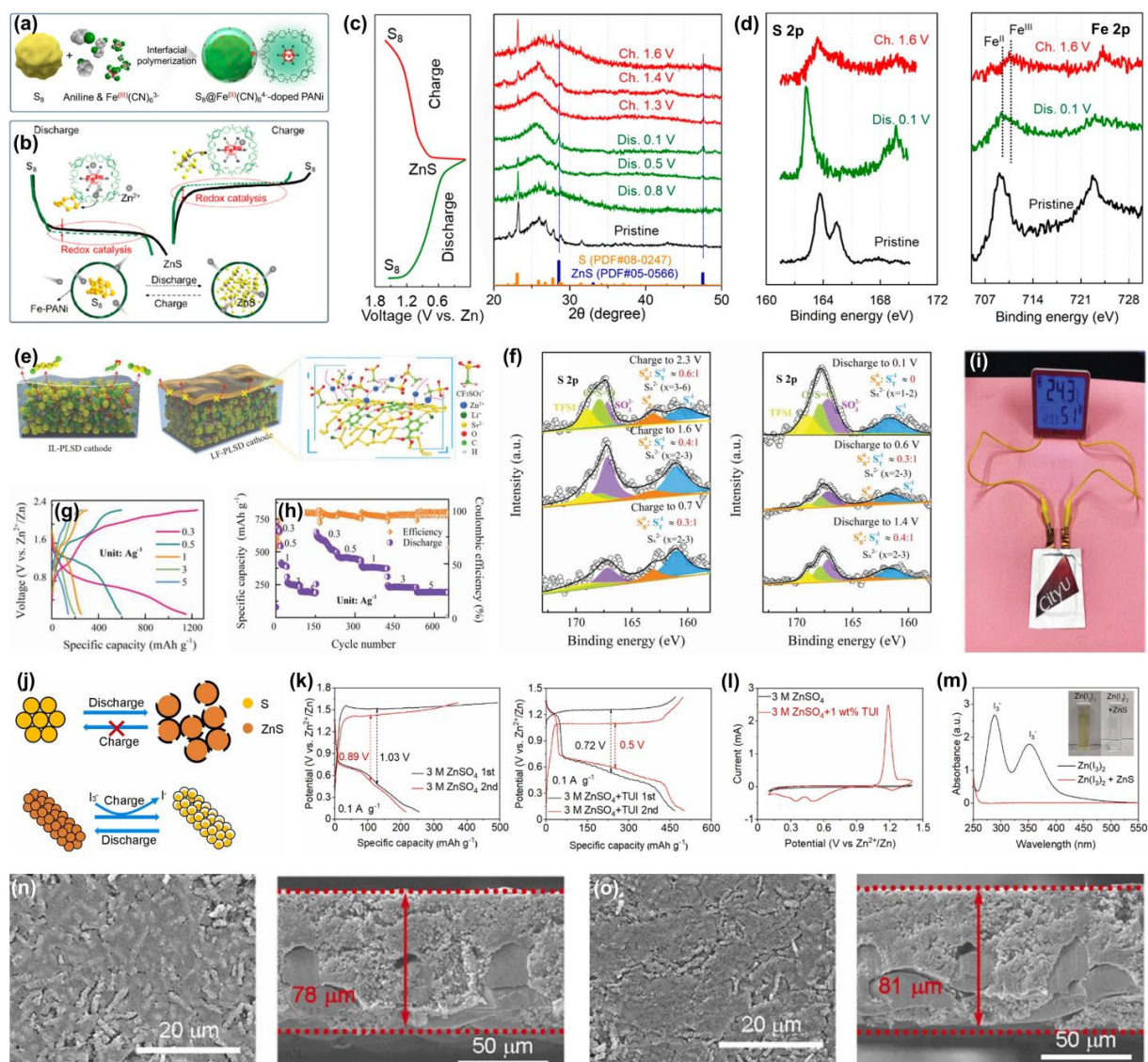


**Figure 8.** (a) Schematic of the synthesis process for S@Fe-PANI; (b) schematic of S redox conversion in AZSBs based on the S@Fe-PANI cathode; (c) ex situ XRD patterns and (d) XPS spectra (S 2p and Fe 2p) of the S@Fe-PANI at different states (reproduced with permission from Ref. [61]. Copyright 2021, American Chemical Society). (e) Illustration of the PLSD coated with IL or LF; (f) XPS spectra (S 2p) of the Zn anode at different charge/discharge states; (g) GCD curves of the Zn/LF-PLSD cell; (h) rate performance of the Zn/LF-PLSD cell in the high-concentrated electrolyte; (i) a photograph of the quasi-solid Zn/LF-PLSD pouch cell (reproduced with permission from Ref. [89]. Copyright 2020, Wiley-VCH). (j) Illustration of the structure change of S and ZnS cathodes during cycles; (k) initial two GCD curves without and with TUI additive; (l) CV curves of the ZnS cathode without or with TUI additive; (m) UV-Vis spectra of different electrolytes; SEM images of the ZnS cathode (n) at pristine state and (o) after cycles (reproduced with permission from Ref. [90]. Copyright 2022, Elsevier).

A single strategy such as electrolyte modification or cathode optimization may not completely solve all problems in AZSBs; therefore, combining different strategies is appropriate. By selecting ZnS as the cathode material and introducing iodinated thiourea (TUI) as the redox mediator, Huang et al. simultaneously solved the problems of large volume change and slow redox kinetics of S cathodes during the discharge/charge process [90]. Unlike S cathodes, ZnS was completely zincified and contracted at the initial dezincification, creating sufficient space for subsequent volume expansion during zincification, thereby alleviating structural damage to the cathode (Figure 8j). Further, TUI was an effective redox mediator that could reduce the activation barrier of the ZnS cathode, that is, the charging overpotential (from 1.55 V to 1.26 V, Figure 8k). A series of characterization results (Figure 8l,m) revealed the working mechanism of TUI.  $I^-$  was first oxidized to  $I_3^-$ , and it then reacted with ZnS to generate S during the charging process. Moreover, thiourea (TU) could regulate the crystal properties and morphology of the Zn surface to inhibit dendrite growth (Figure 8n,o). Based on these advantages, the ZnS cathode exhibited excellent electrochemical performance with a specific capacity of  $465 \text{ mAh g}_{\text{ZnS}}^{-1}$  (based on the mass of ZnS), achieving a high energy density of  $274 \text{ Wh kg}_{\text{ZnS}}^{-1}$ .

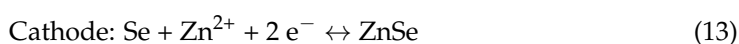
### 3. Aqueous Zn–Se Batteries (AZSeBs)

The Se cathode possesses a considerably higher conductivity than the S cathode ( $1 \times 10^{-3} \text{ S m}^{-1}$ ), with a comparable volumetric specific capacity [91–96]. Therefore, AZSeBs based on Se cathodes have received considerable attention. Currently, research on AZSeBs is in the initial stage, mainly focusing on electrolyte modification and cathode optimization. This section comprehensively describes the research on improving the performance of AZSeBs, along with their working mechanisms.

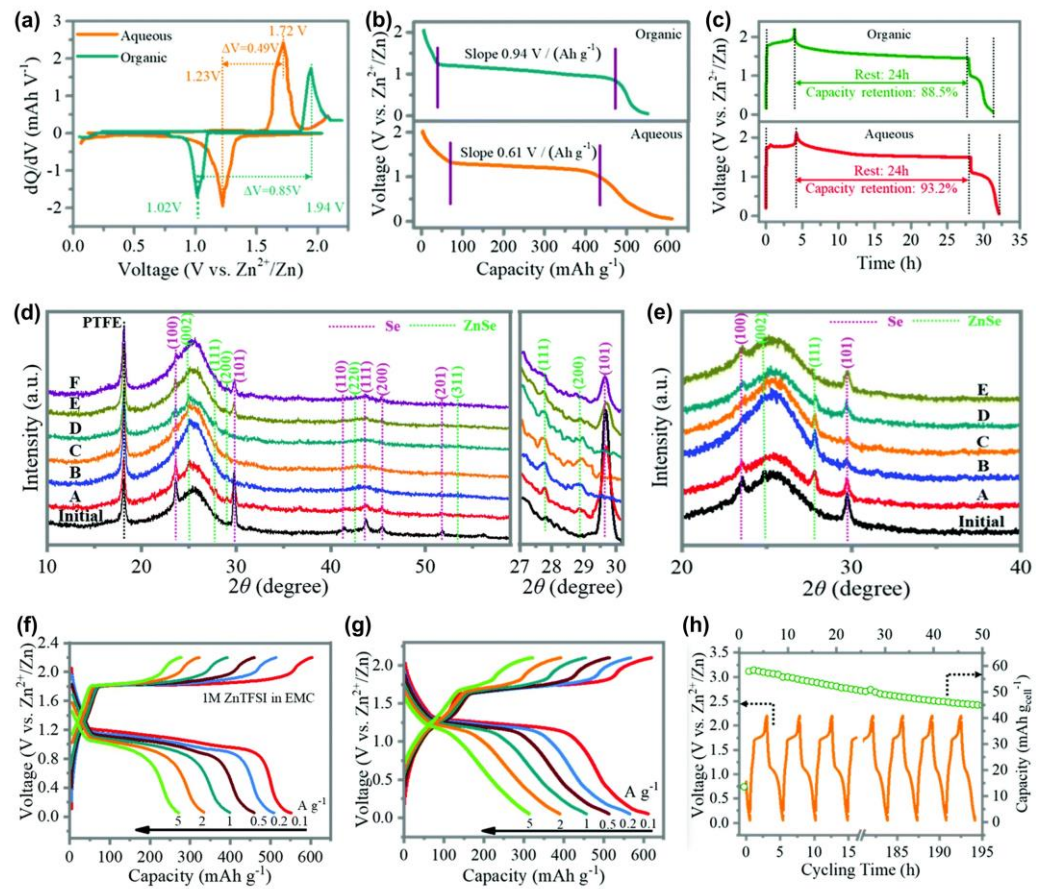
#### 3.1. Electrolyte Modification for AZSeBs

##### 3.1.1. Choice of Electrolyte for AZSeBs

Zhi et al. constructed new conversion-type AZSeBs, which exhibited good performance in both organic and aqueous electrolytes owing to the highly reversible redox reaction between Se and ZnSe [65]. To weaken the influence of interfacial charge transfer and avoid desolvation issues, Se/ordered mesoporous carbon (Se/CMK-3) composites were employed as the cathodes in both organic and aqueous electrolytes. The performance of AZSeBs in the two systems has been studied and compared. Compared to the organic system (ethyl methyl carbonate, EMC electrolyte), the aqueous system exhibited a lower polarization voltage (0.49 V vs. 0.85 V, Figure 9a) and showed a flatter discharge plateau ( $0.61 \text{ V}/(\text{Ah g}^{-1})$  vs.  $0.94 \text{ V}/(\text{Ah g}^{-1})$ , Figure 9b) caused by the high ionic conductivity of the aqueous electrolyte, thus ensuring efficient conversion kinetics. The aqueous system exhibited better capacity retention (93.2% vs. 88.5%, Figure 9c) in self-discharge tests because of the negligible polyselenide dissolution in the aqueous electrolyte. Ex situ XRD results (Figure 9d,e) revealed that the reaction mechanism of the two systems was the same, with a reversible reaction between Se and ZnSe:



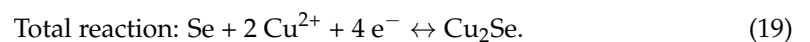
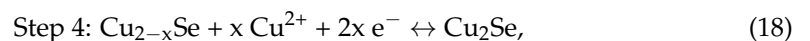
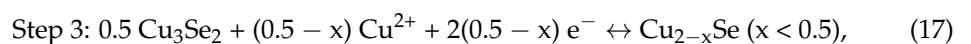
Based on such a conversion mechanism, the AZSeBs delivered a high capacity ( $551 \text{ mAh g}_{\text{Se}}^{-1}$  (based on the mass of Se) in EMC,  $611 \text{ mAh g}_{\text{Se}}^{-1}$  in aqueous electrolyte, at  $100 \text{ mA g}^{-1}$ , Figure 9f,g), high rate performance, and long cycling life in both organic and aqueous systems. Furthermore, the pouch cell was assembled and exhibited stable cycling and remarkable energy densities of  $85.9 \text{ Wh kg}_{\text{cell}}^{-1}$  and  $153.6 \text{ Wh L}_{\text{cell}}^{-1}$  (Figure 9h).



**Figure 9.** Comparison of (a)  $dQ/dV$  of the discharge-charge curves, (b) plateau slopes, and (c) self-discharge behaviors of AZSeBs in organic and aqueous electrolytes; ex situ XRD patterns of AZSeBs in (d) organic and (e) aqueous electrolytes; GCD curves of AZSeBs at different rates in (f) organic and (g) aqueous electrolytes; (h) cycling performance of the pouch cell (reproduced with permission from Ref. [65]. Copyright 2021, Royal Society of Chemistry).

### 3.1.2. Choice of Electrolyte Additive for AZSeBs

Like AZSBs, the mechanism of the solid–solid conversion between Se and ZnSe in AZSeBs slows the kinetics of the conversion reaction. Therefore, the strategy of changing the two-electron conversion to the four-electron conversion by introducing the charge carrier is effective for improving the capacity and kinetics of AZSeBs. Qu et al. designed an aqueous Se cathode chemistry with redox-active  $\text{Cu}^{2+}$  as the charge carrier [68]. In situ XRD (Figure 10a) and other characterization results revealed that the Se cathode with  $\text{Cu}^{2+}$  as the charge carrier underwent four-electron reactions through the sequential conversion reaction  $\text{Se} \leftrightarrow \text{CuSe} \leftrightarrow \text{Cu}_3\text{Se}_2 \leftrightarrow \text{Cu}_{2-x}\text{Se} \leftrightarrow \text{Cu}_2\text{Se}$  (Figure 10b), thus yielding a high theoretical specific capacity of  $1350 \text{ mAh g}_{\text{Se}}^{-1}$ . The following are the reaction processes:



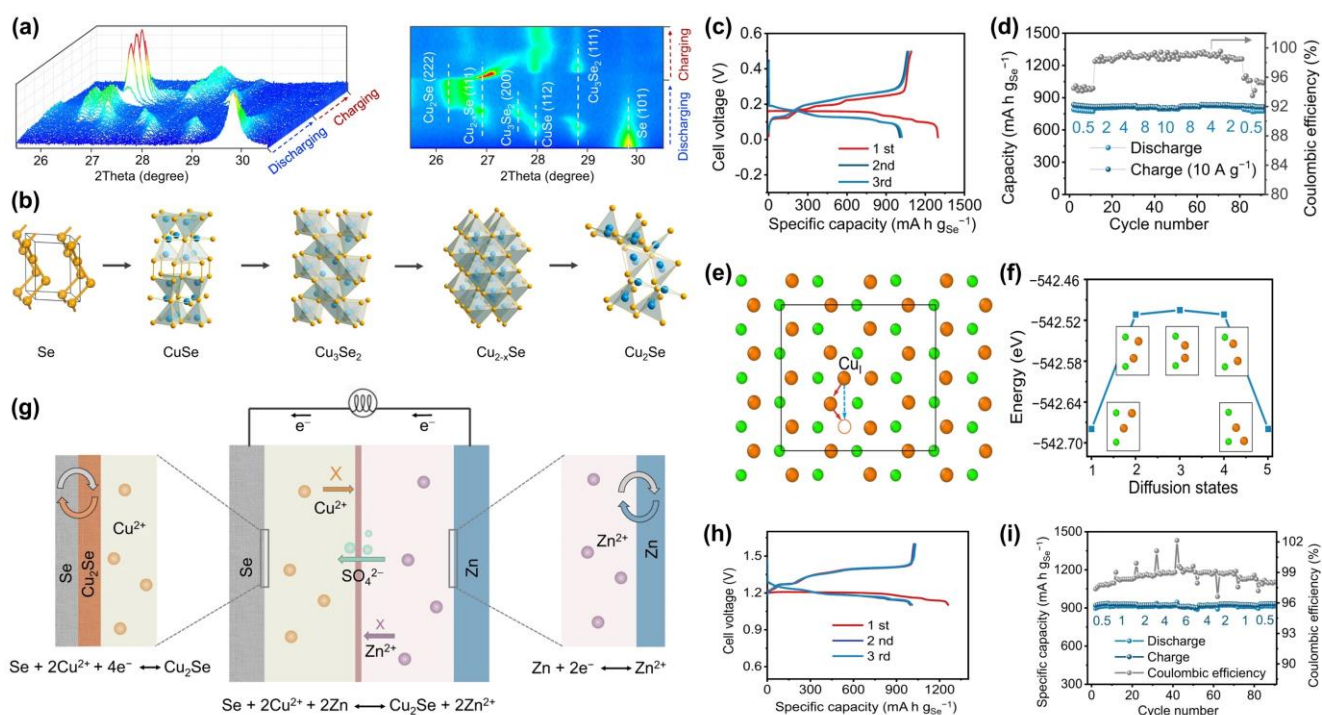
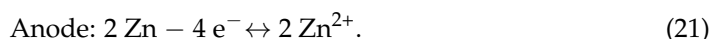
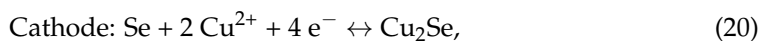


**Figure 10.** (a) In situ XRD patterns and (b) structure evolution of the Se cathode in AZSeBs during cycles; (c) GCD curves of the initial three cycles and (d) fast-charging rate performance of the Cu || Se cell; (e) the top view of CuSe with a Cu<sup>2+</sup> embedded; (f) energy barrier of Cu<sup>2+</sup> diffusion in CuSe; (g) schematic of the Zn || Se full cell; (h) GCD curves of the initial three cycles and (i) fast-charging rate performance of the Zn || Se full cell (reproduced with permission from Ref. [68]. Copyright 2022, Springer Nature).

Based on this four-electron reaction mechanism, the Cu | 0.5 M CuSO<sub>4</sub> | Se@C coin cells exhibited superior capacity (Figure 10c) and high rate performance (Figure 10d). The high rate performance was mainly attributed to the rapid migration of Cu<sup>2+</sup> in this system. The density functional theory (DFT) results indicated that Cu<sup>2+</sup> possessed a relatively low diffusion barrier of 0.174 eV during the diffusion process (Figure 10e,f), which was conducive to improving the fast charge/discharge performance. The Zn || Se full cells were assembled using an electrolyte consisting of 0.5 M ZnSO<sub>4</sub> and 0.5 M CuSO<sub>4</sub> (Figure 10g). The anion exchange membrane was employed to block the direct contact and spontaneous reaction between Cu<sup>2+</sup> and Zn metal. The SO<sub>4</sub><sup>2-</sup> in the electrolyte acted as charge balance and could move through the membrane. The reaction processes of full cells are as follows:



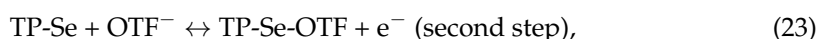
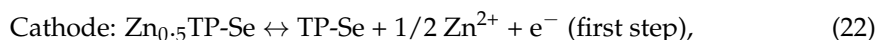
The full cells delivered a high initial capacity of 1263 mA h g<sub>Se</sub><sup>-1</sup> at 0.5 A g<sup>-1</sup> with a stable discharge plateau of 1.2 V (Figure 10h). More importantly, when the charge current was set to 6 A g<sup>-1</sup>, the full cells exhibited a stable discharge capacity of ~900 mA h g<sub>Se</sub><sup>-1</sup>, independent of the current densities, demonstrating excellent rate performance (Figure 10i).

### 3.2. Cathode Optimization for AZSeBs

To avoid serious deterioration of the reaction kinetics, improve Se utilization, and improve cycling life under high Se mass loadings, Zhi et al. proposed an electrocatalytic Se redox reaction strategy, in which the synergistic effect of Cu and electroactive Co sites inside the porous channel structure of the Cu[Co(CN)<sub>6</sub>] host could effectively confine and catalytically convert Se, thereby promoting Se utilization and the conversion

kinetics (Figure 11a) [97]. For Se oxidation, the Cu[Co(CN)<sub>6</sub>] host exhibited the highest current density response (corresponding to the smallest Tafel slope ( $\eta$ ) of 188.06 mV dec<sup>-1</sup>, Figure 11b), the highest tendency for Zn–Se bond breakage, and the smallest decomposition energy barrier of ZnSe (1.83 eV, Figure 11c), indicating the best conversion kinetics of the Cu[Co(CN)<sub>6</sub>] electrocatalyst for Se oxidation. For Se reduction, the Cu[Co(CN)<sub>6</sub>] host exhibited the highest half-wave potential and diffusion-limited current density (1.11 V and 5.53 mA cm<sup>-2</sup>, Figure 11d), the corresponding smallest  $\eta$  of 95.23 mV dec<sup>-1</sup>, and the lowest activation energy of 1.63 kJ mol<sup>-1</sup> (Figure 11e), suggesting the fastest conversion kinetics of the Cu[Co(CN)<sub>6</sub>] host for Se reduction. Accordingly, the Ah-level pouch cell (~1350 mAh) with high Se mass loading (~12.3 mg cm<sup>-2</sup>) exhibited high Se utilization (83.3%) and decent cycling stability (89.4% maintained after 400 cycles, Figure 11f).

Current aqueous Zn batteries generally deliver low discharge voltages, partly owing to the limited high-voltage cathode materials. Chalcogen cathodes undergoing positive valence conversions could offer high discharge voltages in batteries; nevertheless, as the chalcogen elements (O, S, and Se) are electron acceptors, such highly reversible reactions are difficult to realize. Zhi et al. designed a high-voltage organic triphenylphosphine–Se (TP–Se) cathode by combining Se with TP-based structures possessing strong electron-withdrawing groups (Figure 11g) [69]. As shown in the electrostatic potential (ESP) mappings (Figure 11h), the surface charge densities of chalcogens in the TP structure were significantly lower than that of their elemental substances, and the calculated ESPs were –49.3 kcal mol<sup>-1</sup>, –34.6 kcal mol<sup>-1</sup>, and –12.7 kcal mol<sup>-1</sup> for the P = O, P = S, and P = Se bonds, respectively. According to the principle that sites with more positive ESPs are more inclined toward nucleophilic reactions, the attraction of TP–Se to anions during charging significantly increased, potentially causing the positive valence conversion of Se in the TP structure. Ex situ Raman (Figure 11i) and XPS (Figure 11j) results during the charge/discharge process verified this reasonable speculation; the TP–Se cathode underwent conversion from (TP–Se)<sup>-</sup> to (TP–Se)<sup>0</sup> and to (TP–Se)<sup>+</sup> with the assistance of Zn<sup>2+</sup> and OTF<sup>-</sup>, indicating that both n-type and p-type reactions occurred at the TP–Se cathode. The following are the reaction processes:



Based on such a conversion mechanism, the AZSeBs exhibited a high discharge plateau of 1.96 V with a high plateau contribution of 71.2%, long cycling lifespan (85.3% maintained after 4300 cycles), and high rate performance (138 mAh g<sub>Se</sub><sup>-1</sup> at 30 A g<sup>-1</sup>).

To improve the performance of AZCBs, Wang et al. introduced Se into the S cathode to reasonably balance the characteristics of S and Se, and proposed a Se–S solid solution (Se<sub>x</sub>S<sub>y</sub>) as the cathode for AZCBs (Figure 12a) [98]. As shown in Figure 12b, the addition of Se improved the electrical conductivity of Se<sub>x</sub>S<sub>y</sub>, which increased with the increase of Se content. By optimizing the Se content, the SeS<sub>5.76</sub> cathode delivered a high capacity (1222 mAh g<sup>-1</sup> at 0.2 A g<sup>-1</sup>) with a flat discharge plateau of 0.71 V (Figure 12c–e), high rate capability (713 mAh g<sup>-1</sup> at 5 A g<sup>-1</sup>), and long cycling lifespan (75% maintained after 500 cycles). Ex situ XRD and XPS results at different charge/discharge states revealed that the discharge process determined the reaction kinetics, in which the Se<sub>x</sub>S<sub>y</sub> cathode (SeS<sub>5.76</sub>) was converted into ZnS and ZnSe. Moreover, the DFT results showed that introducing Se could adjust the electron density difference (Figure 12f), band structure, and reaction energy of the S cathode and discharge products, thereby improving the conductivity and reactivity of the S cathode and promoting the electrochemical reaction with the Zn anode.

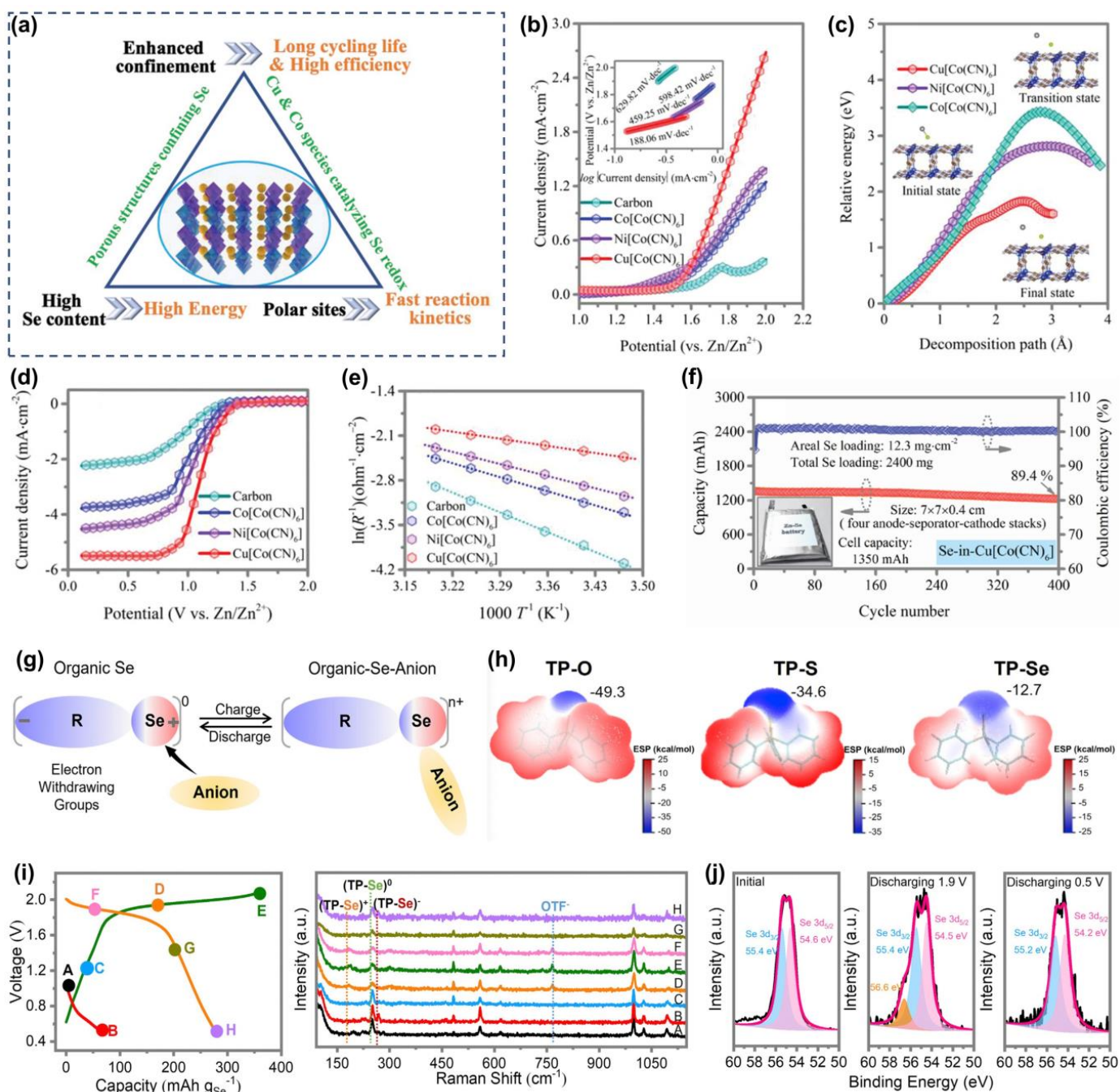


**Figure 11.** (a) Illustration of the cathode design for AZSeBs; (b) LSV curves and corresponding Tafel plots of  $(\text{Cu}/\text{Ni}/\text{Co})[\text{Co}(\text{CN})_6]$  for Se oxidation; (c) decomposition energy barrier of ZnSe on different hosts; (d) LSV curves of  $(\text{Cu}/\text{Ni}/\text{Co})[\text{Co}(\text{CN})_6]$  for Se reduction; (e) activation energies of different hosts; (f) cycling performance of the Ah-level pouch cell with high Se mass-loading (reproduced with permission from Ref. [97]. Copyright 2022, Wiley-VCH). (g) Schematic of the strategy for positive valence conversion of Se; (h) ESP mappings of TP-O/S/Se; (i) GCD curve at  $0.5 \text{ A g}^{-1}$  and corresponding ex situ Raman spectra; (j) ex situ XPS spectra of Se 3d at different states (reproduced with permission from Ref. [69]. Copyright 2022, Elsevier).

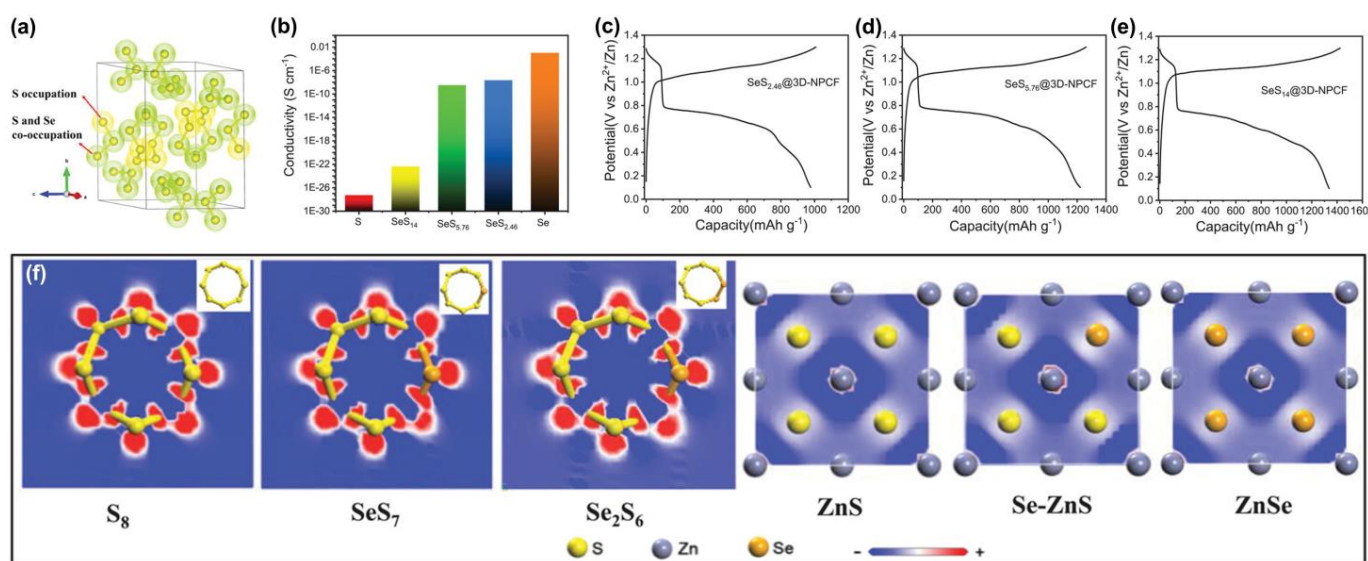


**Figure 12.** (a) Crystal structure of  $\text{Se}_x\text{S}_y$  ( $\text{Se}_{1.1}\text{S}_{6.9}$ ); (b) conductivities of different  $\text{Se}_x\text{S}_y$ ; (c–e) GCD curves of different  $\text{Se}_x\text{S}_y$  cathodes at  $0.2 \text{ A g}^{-1}$ ; (f) electron density differences for different charge and discharge products (reproduced with permission from Ref. [98]. Copyright 2021, Wiley-VCH).

#### 4. Aqueous Zn–Te Batteries (AZTeBs)

Among the three chalcogen elements (S, Se, and Te), Te possesses the highest conductivity ( $2 \times 10^2 \text{ S m}^{-1}$ ) and considerable theoretical capacity [99–103]. Hence, AZTeBs based on Te cathodes have also received research attention. Currently, research on this energy storage system is in its infancy, mainly focusing on mechanism investigation and performance optimization, which are described in this section.

##### 4.1. Mechanism Investigation for AZTeBs

To improve the electrochemical performance of aqueous Zn batteries, Zhi et al. first reported conversion-type AZTeBs with Te as the cathode and Zn as the anode [66]. Ex situ XRD (Figure 13a) and XPS results during charge/discharge process revealed that the Te cathode underwent a two-step reversible conversion of Te to  $\text{ZnTe}_2$  and  $\text{ZnTe}_2$  to  $\text{ZnTe}$  (Figure 13b). The reaction processes are as follows:



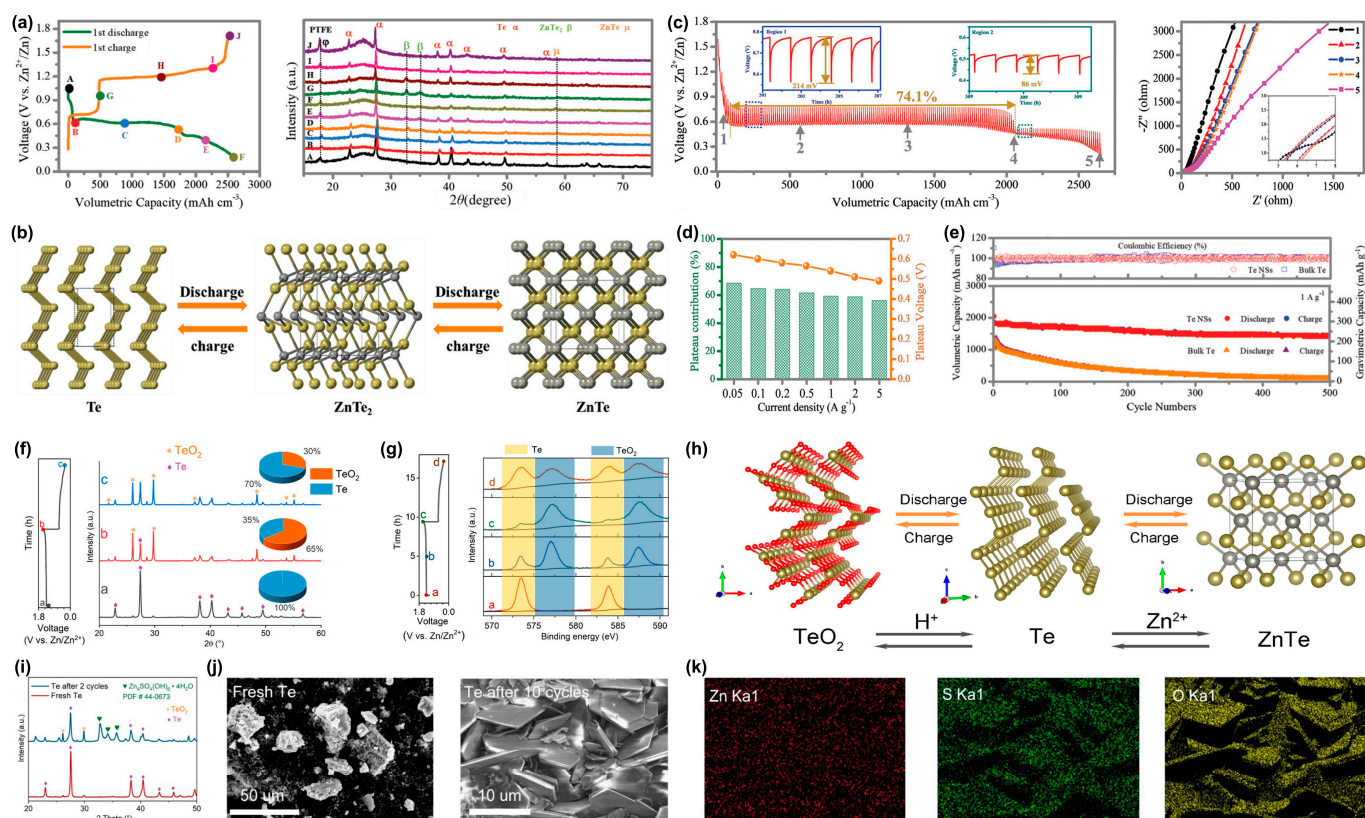
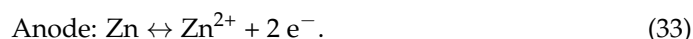
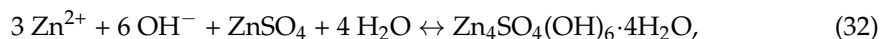
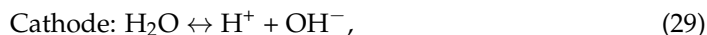


**Figure 13.** (a) GCD curve at 0.05 A g<sup>-1</sup> and corresponding ex situ XRD patterns; (b) schematic of phase transformation of the Te cathode in AZTeBs; (c) galvanostatic intermittent titration technique (GITT) profiles of AZTeBs and corresponding electrochemical impedance spectroscopy (EIS) curves at different discharge states; (d) plateau contribution and voltage plateau at different current densities; (e) cycling stability of AZTeBs (reproduced with permission from Ref. [66]. Copyright 2020, Wiley-VCH). GCD curve at 50 mA g<sup>-1</sup> and corresponding (f) ex situ XRD patterns and (g) ex situ XPS spectra (Te 3d<sub>3/2</sub> and Te 3d<sub>5/2</sub>); (h) schematic of the reaction mechanism; (i) XRD patterns and (j) SEM images of fresh Te and Te after cycles; (k) EDS mappings (Zn, S, and O) of Te after cycles (reproduced with permission from Ref. [104]. Copyright 2021, American Chemical Society).

According to this conversion mechanism, the AZTeBs delivered a high specific capacity of 2619 mAh cm<sup>-3</sup> at 0.05 A g<sup>-1</sup>, with 74.1% attributed to the capacity contribution of the first conversion (Te to ZnTe<sub>2</sub>) with a flat discharge voltage plateau (Figure 13c). Interestingly, the discharge plateau was still flat and the plateau contribution remained 56.2% even at 5 A g<sup>-1</sup> (Figure 13d), which could be attributed to the high conductivity of Te, ensuring the fast reaction kinetics of Te with ZnTe<sub>2</sub>. Moreover, the AZTeBs exhibited good cycling stability (82.8% maintained after 500 cycles, Figure 13e), which was attributed to the elimination of the shuttle effect due to solid–solid conversion mechanism. Furthermore, the quasi-solid-state cell was assembled, and it exhibited high flexibility and a long lifespan.

Cui et al. further investigated the mechanism of AZTeBs because they found that the existence of H<sup>+</sup> and Zn<sup>2+</sup> in H<sub>2</sub>O could improve the redox reactions in aqueous electrolytes [104]. They used ex situ XRD, XPS, and SEM to study the structural evolution of cathodes during the charge/discharge process, revealing the sequential conversion mechanism of H<sup>+</sup>/Zn<sup>2+</sup> with 6 e<sup>-</sup> transfer in AZTeBs. The ex situ XRD and XPS results (Figure 13f,g) indicated two different redox processes, corresponding to TeO<sub>2</sub> ↔ Te and Te ↔ ZnTe (Figure 13h) within the electrochemical window of conventional aqueous electrolytes. Specifically, the fully charged TeO<sub>2</sub> reacted with H<sup>+</sup> to generate Te, and the newly formed Te further reacted with Zn<sup>2+</sup> to generate ZnTe during the discharge process. The XRD patterns after cycles (Figure 13i) showed that Zn<sub>4</sub>SO<sub>4</sub>(OH)<sub>6</sub>·4H<sub>2</sub>O formed on the cathode during discharging, which was consistent with the SEM images and corresponding

EDS mappings (Figure 13j,k). Therefore, the overall reaction processes in ZnSO<sub>4</sub> aqueous electrolyte are as follows:



#### 4.2. Performance Optimization for AZTeBs

Wang et al. designed a type of AZTeBs that worked stably at a high temperature of 100 °C by introducing 1,5-pentanediol (PD) into the aqueous Zn(OTf)<sub>2</sub>-H<sub>2</sub>O electrolyte [105]. As a crowding agent [106], PD could inhibit the reactivity of H<sub>2</sub>O by strengthening O–H bonds and reducing the H<sub>2</sub>O content in the solvation sheath of Zn<sup>2+</sup>, while maintaining the flame retardancy of the aqueous electrolyte, which was beneficial to uniform Zn deposition at high temperatures. The radial distribution functions (RDFs) of the agents coordinated to Zn<sup>2+</sup> in Zn(OTf)<sub>2</sub>-H<sub>2</sub>O and Zn(OTf)<sub>2</sub>-H<sub>2</sub>O/PD electrolytes at 25 °C (Figure 14a,b) indicated that PD repulsed large amounts of H<sub>2</sub>O in the Zn<sup>2+</sup> solvation sheath of the Zn(OTf)<sub>2</sub>-H<sub>2</sub>O/PD electrolyte, significantly reducing the coordination number of Zn–O(H<sub>2</sub>O) from 5.0 (83.7%) to 1.8 (29.2%), which was conducive to suppressing the severe side reactions due to the H<sub>2</sub>O molecules in the solvation sheath of Zn<sup>2+</sup>. More importantly, the changes in the RDFs at 100 °C were consistent with those at 25 °C (Figure 14c,d), validating the above conclusions. The asymmetric Zn || Ti cell based on the Zn(OTf)<sub>2</sub>-H<sub>2</sub>O/PD electrolyte stably operated over 400 cycles at 100 °C with a high average CE of 98.1% (Figure 14e). Moreover, the symmetric Zn || Zn cell also achieved high cycling stability of 500 cycles at 1 mA cm<sup>−2</sup> with 0.5 mAh cm<sup>−2</sup> (Figure 14f).

Furthermore, the AZTeBs based on the Zn(OTf)<sub>2</sub>-H<sub>2</sub>O/PD electrolyte were assembled and exhibited excellent electrochemical performance at 100 °C. In the CV curves of the AZTeBs, the distinct cathodic and anodic peaks stemmed from the redox reactions between Te and ZnTe with ZnTe<sub>2</sub> as the intermediate (Figure 14g). The GCD curves (Figure 14h) indicated the problem of AZTeBs using the conventional Zn(OTf)<sub>2</sub>-H<sub>2</sub>O electrolyte at high temperatures, i.e., the ultrahigh charging capacity of the Te cathode (720 mAh g<sup>−1</sup>) exceeding the theoretical capacity (425 mAh g<sup>−1</sup>), which could be due to the decomposition of the electrolyte during charging. On the contrary, the AZTeBs based on the Zn(OTf)<sub>2</sub>-H<sub>2</sub>O/PD electrolyte delivered a reversible capacity of 386.4 mAh g<sup>−1</sup> at 0.5 C with approximately 100% CE. Meanwhile, the AZTeBs based on the Zn(OTf)<sub>2</sub>-H<sub>2</sub>O/PD electrolyte exhibited stable cycling performance at 100 °C (195.7 mAh g<sup>−1</sup> maintained after 100 cycles at 2 C, Figure 14i). Moreover, a temperature sensor was powered by the AZTeBs based on the Zn(OTf)<sub>2</sub>-H<sub>2</sub>O/PD electrolyte, indicating their practical application potential at extremely high temperatures (Figure 14j).

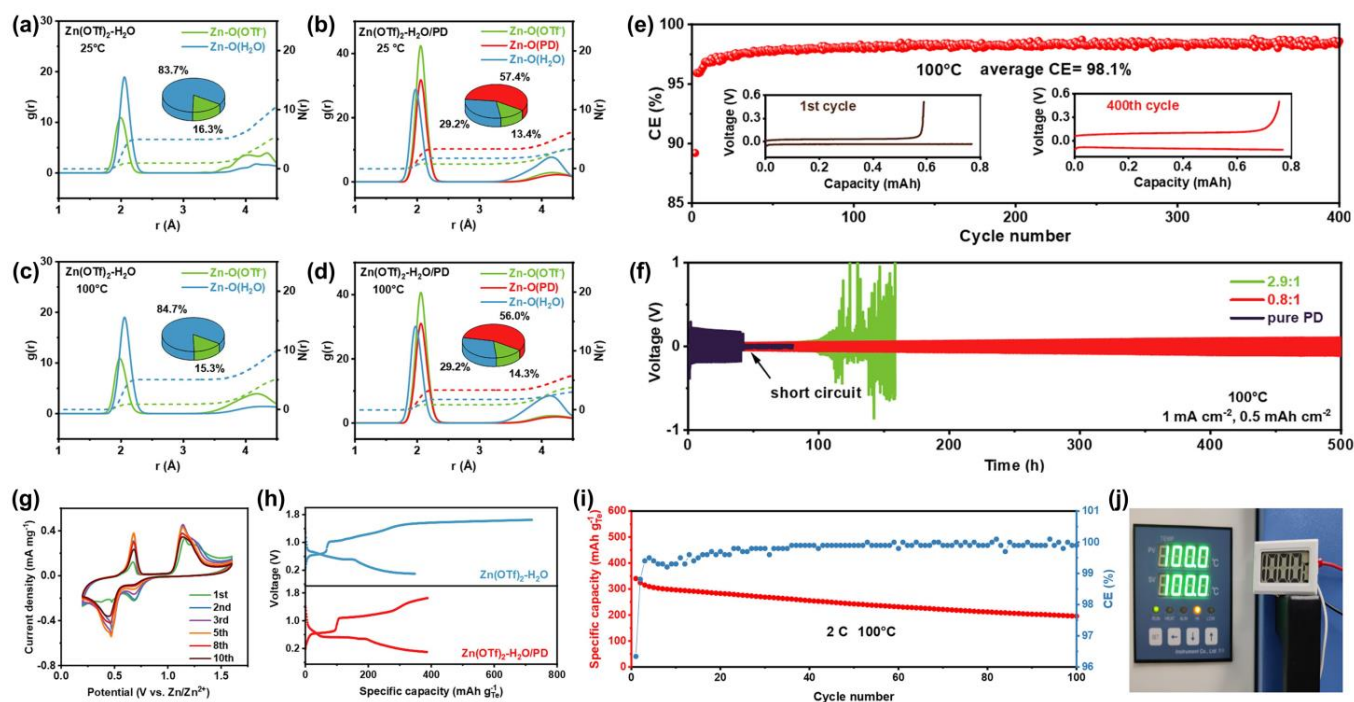


**Figure 14.** (a–d) RDFs of the agents coordinated to Zn<sup>2+</sup> in different electrolytes at 25 °C and 100 °C; (e) CE evaluation of the asymmetric Zn || Ti cell and (f) cycling test of the symmetric Zn || Zn cell at 100 °C; (g) CV curves of the AZTeBs at 100 °C; (h) GCD curves of the AZTeBs in different electrolytes at 100 °C; (i) cycling performance of the AZTeBs based on the Zn(O Tf)<sub>2</sub>-H<sub>2</sub>O/PD electrolyte at 100 °C; (j) a photograph of a temperature sensor powered by the AZTeBs at 100 °C (reproduced with permission from Ref. [105]. Copyright 2022, American Chemical Society).

## 5. Conclusions and Perspective

AZMBs are considered as promising candidates for next-generation energy storage systems, attributed to the natural abundance, low redox potential, and high theoretical capacity of Zn. However, typical cathode materials for AZMBs are mainly based on ion-insertion electrochemistry, which can only deliver limited capacity; therefore, the performance of AZMBs is not fully realized. The conversion-type AZCBs have attracted research attention because they combine the advantages of chalcogen cathodes (S, Se, and Te) and Zn anodes to considerably improve the capacity and energy density. However, several issues have hindered the commercialization of AZCBs, such as poor conductivity, volume changes, and sluggish reaction kinetics of chalcogen cathodes, as well as corrosion, hydrogen evolution, and dendrite growth on Zn anodes. To address these challenges, several efforts have been made to rationally optimize AZCBs, although research on AZCBs is still in its infancy. This review comprehensively describes the recent progress related to AZCBs, particularly considering the following aspects. Table 1 provides a comprehensive summary.

**Table 1.** Comprehensive comparison of electrochemical properties among the typical AZCBs.

Cathodes for Systems	Electrolytes	Full Batteries			Energy Densities (Wh kg <sup>-1</sup> )	Ref.
		Rate Performance (mAh g <sup>-1</sup> / mA g <sup>-1</sup> )	Discharge Plateau (V/mA g <sup>-1</sup> )	Cycling Performance (mAh g <sup>-1</sup> /cycles/mA g <sup>-1</sup> )		
KB-S for AZSBs	1 M ZnCl <sub>2</sub>	1668/50 >1500/1000	0.7/50	Primary battery	1083.3	[80]
CMK-3@S for AZSBs	3 M Zn(OTF) <sub>2</sub>	699/200 415/1000	0.24/200	270/100/1000	–	[64]
S@CB for AZSBs	0.5 M ZnCl <sub>2</sub> + 0.5 M LiCl in DES	846/500 (with 10% AN additive) 569.3/500, 122.6/4000 (with 5% AN additive)	~0.7/500	126.1/400/1000 (with 5% AN additive)	259	[83]
S@CNTs-50 for AZSBs	1 M Zn(AC) <sub>2</sub> + PEG additive	1116/100 774/1000	~0.8 /100	645/300/1000	–	[63]
S/AC for AZSBs	Catholyte: 0.5 M CuSO <sub>4</sub> Anolyte: 0.5 M ZnSO <sub>4</sub>	2000/50	1.15/50	>1500/110/1000	547	[67]
S@C for AZSBs	Catholyte: Gelatin/CuSO <sub>4</sub> Anolyte: Gelatin/ZnSO <sub>4</sub>	2063/100 938/2000	~1.2/100	1442/100/500	2372	[62]
S@C for AZSBs	Catholyte: PAM/CuSO <sub>4</sub> Anolyte: PAM/ZnSO <sub>4</sub>	48 mAh cm <sup>-2</sup> /9.6 mg cm <sup>-2</sup> cathode loading	Step 1: 1.15 Step 2: 1.05 (1 mA cm <sup>-2</sup> )	6 mAh cm <sup>-2</sup> /100 /1 mA cm <sup>-2</sup>	47.6 mWh cm <sup>-2</sup>	[84]
S@CNTs-50 for AZSBs	1 M Zn(AC) <sub>2</sub> + 0.05 wt% I <sub>2</sub>	1105/100 407/4000	0.5/100	302/225/1000	502	[74]
HCS/S-53.7 for AZSBs	Zn(OTF) <sub>2</sub> /G4/I <sub>2</sub>	1140/500 472/5000	~0.5/500	349/600/4000	–	[73]
S@Fe-PANi for AZSBs	PVA/ZnSO <sub>4</sub>	1205/200 705/2000	0.58/200	604/500/2000	720	[61]
LF-PLSD for AZSBs	1 M Zn(TFSI) <sub>2</sub>	1148/300 489/500	0.9–1.5/300	235/700/1000 247/900/1000 (quasi-solid)	724.7	[89]
ZnS@CF for AZSBs	3 M ZnSO <sub>4</sub> + 1 wt% TUI	465/100 390/2000	0.59/100	226/300/2000	274	[90]
Se/CMK-3 for AZSeBs	1 M Zn(TFSI) <sub>2</sub> in EMC 2M Zn(TFSI) <sub>2</sub> in water + PEG	551/100, 282/5000 611/100, 315/5000	~1.2/100 0.94 V/(Ah g <sup>-1</sup> ) ~1.25/100 0.61 V/(Ah g <sup>-1</sup> )	334/500/1000 365/1000/1000	581 751	[65]
Se@C for AZSeBs	Catholyte: 0.5 M CuSO <sub>4</sub> Anolyte: 0.5 M ZnSO <sub>4</sub>	~900/500 ~900/6000	1.2/500	~900 (~100%)/400/2000	1500 mWh g <sup>-1</sup>	[68]
Se-in-Cu[Co(CN) <sub>6</sub> ] for AZSeBs	4 M Zn(OTf) <sub>2</sub> / PEO	664.7/200 430.6/10,000	~1.2/200	~500(90.6%)/6000/5000	728.9	[97]
TP-Se for AZSeBs	1 M Zn(OTf) <sub>2</sub> + AN	317/500 138/30,000	1.96/500	211/4300/2000	621.3	[69]
SeS <sub>5.76</sub> @3D-NPCF for AZSeBs	3 M ZnSO <sub>4</sub> + 0.1 wt% I <sub>2</sub>	1222/200 713/5000	0.71/200	527/500/4000	867.6	[98]
Te nanosheets for AZTeBs	1 M ZnSO <sub>4</sub>	2619 mAh cm <sup>-3</sup> /50 1185 mAh cm <sup>-3</sup> /5000	Step 1: 0.59/50 Step 2: 0.48/50	1546 mAh cm <sup>-3</sup> /500/1000	1504 Wh L <sup>-1</sup>	[66]
Te for AZTeBs	1 M ZnSO <sub>4</sub>	460/50	~0.6/50	162/50/50	–	[104]
Te-G-CNT for AZTeBs	Zn(OTf) <sub>2</sub> -H <sub>2</sub> O/PD	386.4/212	~0.5/212	195.7/100/850 (100 °C)	–	[105]

- (1) Research on AZSBs mainly includes electrolyte modification and cathode optimization. As for the electrolyte choice, how factors such as the solute, concentration, and solvent influence the performance of AZSBs are summarized. Regarding electrolyte additive selection, two types of electrolyte additives are described in detail, depending on whether to change the two-electron reaction processes of AZSBs. For cathode optimization, various strategies and their mechanisms are thoroughly discussed.
- (2) Research on AZSeBs mostly involves electrolyte modification and cathode optimization. In terms of electrolyte choice, the similarities and differences among AZSeBs in organic and aqueous electrolytes are compared, and the working mechanisms are presented. As for the choice of the electrolyte additive, the strategy and corresponding mechanism of changing the two-electron reaction to the four-electron reaction are

de-tailed. For cathode optimization, different strategies and their mechanisms are comprehensively discussed.

- (3) >Research on AZTeBs focuses on mechanism investigation and performance optimization. For mechanism investigation, two systems are proposed and compared according to different working mechanisms. For performance optimization, a system operating at extremely high temperatures is described and its mechanism is thoroughly analyzed.

Although research on AZCBs has made considerable progress, it is still in its infancy, and the following blind spots and bottlenecks need to be addressed urgently:

- (1) The mechanism investigations of AZCBs are still not thorough and systematic, and the working mechanism of some systems is not clear. For example, the influence of protons on the working mechanism in insertion-type aqueous batteries is known to be significant [107–110]. However, there are different opinions about whether protons are involved in the redox reactions of conversion-type AZCBs, which must be further explored by combining theoretical calculations and experimental evidence.
- (2) Low discharge voltage is a common issue for AZCBs, but there are few studies on increasing discharge voltage, which affects the commercialization process of AZCBs. Therefore, improving the voltage output is an important future development direction of AZCBs, which requires further in-depth and systematic research.
- (3) Most of the current strategies are only proposed for one side (cathode or anode) of the AZCBs, and the issues existing in the cathode and anode cannot be solved simultaneously, thus probably affecting the further development of AZCBs. Developing multifunctional strategies or combining different strategies to solve both these problems at the same time may be a direction worth exploring.
- (4) Unified and standardized testing protocols should be established for AZCBs, especially in the early stage of development. The lack of unified standards interferes considerably with fair comparisons and will be an obstacle to future research and even commercialization. Moreover, targets for optimizing key parameters, such as capacity, energy density, cycling life, and CE, should be set to facilitate the development of AZCBs for commercial applications.
- (5) The electrochemical test conditions should be closer to the practical application situations (harsher environments), such as increasing the mass loading of cathode materials, increasing the current density, and decreasing the amount of electrolyte. Furthermore, tests using full batteries should be introduced as necessary performance evaluation methods to promote the further development of AZCBs.

Although there are still many challenges facing the research on AZCBs, excellent studies continue to emerge. We believe that with the continuous improvements in various strategies and comprehensive explorations of the mechanisms, AZCBs, which are energy storage systems with broad application prospects, will eventually be commercialized.

**Author Contributions:** Conceptualization, writing—original draft preparation, writing—review and editing, all authors. All authors have read and agreed to the published version of the manuscript.

**Funding:** This research was funded by the National Natural Science Foundation of China (52201201), the State Key Lab of Advanced Metals and Materials (2022Z-11), the Fundamental Research Funds for the Central Universities (00007747, 06500205), and the Initiative Postdocs Supporting Program (BX20190002).

**Data Availability Statement:** No new data were created or analyzed in this study. Data sharing is not applicable to this article.

**Conflicts of Interest:** The authors declare no conflict of interest.

## References

1. Liang, Y.; Dong, H.; Aurbach, D.; Yao, Y. Current status and future directions of multivalent metal-ion batteries. *Nat. Energy* **2020**, *5*, 646–656. [[CrossRef](#)]
2. Cao, L.; Li, D.; Pollard, T.; Deng, T.; Zhang, B.; Yang, C.; Chen, L.; Vatamanu, J.; Hu, E.; Hourwitz, M.J.; et al. Fluorinated interphase enables reversible aqueous zinc battery chemistries. *Nat. Nanotechnol.* **2021**, *16*, 902–910. [[CrossRef](#)] [[PubMed](#)]
3. Zhao, Z.; Sun, M.; Chen, W.; Liu, Y.; Zhang, L.; Dongfang, N.; Ruan, Y.; Zhang, J.; Wang, P.; Dong, L.; et al. Sandwich, vertical-channeled thick electrodes with high rate and cycle performance. *Adv. Funct. Mater.* **2019**, *29*, 1809196. [[CrossRef](#)]
4. Zhao, Z.; Sun, M.; Wu, T.; Zhang, J.; Wang, P.; Zhang, L.; Yang, C.; Peng, C.; Lu, H. A bifunctional-modulated conformal Li/Mn-rich layered cathode for fast-charging, high volumetric density and durable Li-ion full cells. *Nano-Micro Lett.* **2021**, *13*, 118. [[CrossRef](#)] [[PubMed](#)]
5. Zhou, G.; Chen, H.; Cui, Y. Formulating energy density for designing practical lithium-sulfur batteries. *Nat. Energy* **2022**, *7*, 312–319. [[CrossRef](#)]
6. Zhong, C.; Liu, B.; Ding, J.; Liu, X.; Zhong, Y.; Li, Y.; Sun, C.; Han, X.; Deng, Y.; Zhao, N.; et al. Decoupling electrolytes towards stable and high-energy rechargeable aqueous zinc-manganese dioxide batteries. *Nat. Energy* **2020**, *5*, 440–449. [[CrossRef](#)]
7. Zheng, J.; Bock, D.C.; Tang, T.; Zhao, Q.; Yin, J.; Tallman, K.R.; Wheeler, G.; Liu, X.; Deng, Y.; Jin, S.; et al. Regulating electrodeposition morphology in high-capacity aluminium and zinc battery anodes using interfacial metal–substrate bonding. *Nat. Energy* **2021**, *6*, 398–406. [[CrossRef](#)]
8. Zhang, T.; Zhang, L.; Zhao, L.; Huang, X.; Li, W.; Li, T.; Shen, T.; Sun, S.; Hou, Y. Free-standing, foldable V<sub>2</sub>O<sub>3</sub>/multichannel carbon nanofibers electrode for flexible Li-ion batteries with ultralong lifespan. *Small* **2020**, *16*, 2005302. [[CrossRef](#)]
9. Zhang, L.; Pan, Y.; Chen, Y.; Li, M.; Liu, P.; Wang, C.; Wang, P.; Lu, H. Designing vertical channels with expanded interlayers for Li-ion batteries. *Chem. Commun.* **2019**, *55*, 4258–4261. [[CrossRef](#)]
10. Dong, L.; Zhang, L.; Lin, S.; Chen, Z.; Wang, Y.; Zhao, X.; Wu, T.; Zhang, J.; Liu, W.; Lu, H.; et al. Building vertically-structured, high-performance electrodes by interlayer-confined reactions in accordion-like, chemically expanded graphite. *Nano Energy* **2020**, *70*, 104482. [[CrossRef](#)]
11. Zhang, T.; Zhang, L.; Hou, Y. MXenes: Synthesis strategies and lithium-sulfur battery applications. *eScience* **2022**, *2*, 164–182. [[CrossRef](#)]
12. Zhang, L.; Chen, Z.; Dongfang, N.; Li, M.; Diao, C.; Wu, Q.; Chi, X.; Jiang, P.; Zhao, Z.; Dong, L.; et al. Nickel–cobalt double hydroxide as a multifunctional mediator for ultrahigh-rate and ultralong-life Li-S batteries. *Adv. Energy Mater.* **2018**, *8*, 1802431. [[CrossRef](#)]
13. Lu, C.; Li, A.; Li, G.; Yan, Y.; Zhang, M.; Yang, Q.; Zhou, W.; Guo, L. S-decorated porous Ti<sub>3</sub>C<sub>2</sub> MXene combined with in situ forming Cu<sub>2</sub>Se as effective shuttling interrupter in Na-Se batteries. *Adv. Mater.* **2021**, *33*, 2008414. [[CrossRef](#)] [[PubMed](#)]
14. Zhang, Y.; Manaig, D.; Freschi, D.J.; Liu, J. Materials design and fundamental understanding of tellurium-based electrochemistry for rechargeable batteries. *Energy Storage Mater.* **2021**, *40*, 166–188. [[CrossRef](#)]
15. Tang, T.Y.; Zhang, T.; Zhao, L.N.; Zhang, B.; Li, W.; Xu, J.J.; Zhang, L.; Qiu, H.L.; Hou, Y.L. Multifunctional ultrasmall-MoS<sub>2</sub>/graphene composites for high sulfur loading Li-S batteries. *Mater. Chem. Front.* **2020**, *4*, 1483–1491. [[CrossRef](#)]
16. Fang, C.; Li, J.; Zhang, M.; Zhang, Y.; Yang, F.; Lee, J.Z.; Lee, M.; Alvarado, J.; Schroeder, M.A.; Yang, Y.; et al. Quantifying inactive lithium in lithium metal batteries. *Nature* **2019**, *572*, 511–515. [[CrossRef](#)]
17. Zhou, X.; Zhang, Q.; Zhu, Z.; Cai, Y.; Li, H.; Li, F. Anion-reinforced solvation for a gradient inorganic-rich interphase enables high-rate and stable sodium batteries. *Angew. Chem. Int. Ed.* **2022**, *61*, e202205045. [[CrossRef](#)]
18. Yang, H.; He, F.; Li, M.; Huang, F.; Chen, Z.; Shi, P.; Liu, F.; Jiang, Y.; He, L.; Gu, M.; et al. Design principles of sodium/potassium protection layer for high-power high-energy sodium/potassium-metal batteries in carbonate electrolytes: A case study of Na<sub>2</sub>Te/K<sub>2</sub>Te. *Adv. Mater.* **2021**, *33*, 2106353. [[CrossRef](#)]
19. Zhang, T.; Zhang, L.; Zhao, L.; Huang, X.; Hou, Y. Catalytic effects in the cathode of Li-S batteries: Accelerating polysulfides redox conversion. *EnergyChem* **2020**, *2*, 100036. [[CrossRef](#)]
20. He, J.; Lv, W.; Chen, Y.; Wen, K.; Xu, C.; Zhang, W.; Li, Y.; Qin, W.; He, W. Tellurium-impregnated porous cobalt-doped carbon polyhedra as superior cathodes for lithium-tellurium batteries. *ACS Nano* **2017**, *11*, 8144–8152. [[CrossRef](#)]
21. Sun, J.; Du, Z.; Liu, Y.; Ai, W.; Wang, K.; Wang, T.; Du, H.; Liu, L.; Huang, W. State-of-the-art and future challenges in high energy lithium-selenium batteries. *Adv. Mater.* **2021**, *33*, 2003845. [[CrossRef](#)] [[PubMed](#)]
22. Zeng, L.; Li, W.; Jiang, Y.; Yu, Y. Recent progress in Li-S and Li-Se batteries. *Rare Met.* **2017**, *36*, 339–364. [[CrossRef](#)]
23. Liu, Q.; Deng, W.; Sun, C. A potassium-tellurium battery. *Energy Storage Mater.* **2020**, *28*, 10–16. [[CrossRef](#)]
24. Ji, X.; Lee, K.T.; Nazar, L.F. A highly ordered nanostructured carbon-sulphur cathode for lithium-sulphur batteries. *Nat. Mater.* **2009**, *8*, 500–506. [[CrossRef](#)] [[PubMed](#)]
25. Zhang, L.; Liu, Y.; Zhao, Z.; Jiang, P.; Zhang, T.; Li, M.; Pan, S.; Tang, T.; Wu, T.; Liu, P.; et al. Enhanced polysulfide regulation via porous catalytic V<sub>2</sub>O<sub>3</sub>/V<sub>8</sub>C<sub>7</sub> heterostructures derived from metal-organic frameworks toward high-performance Li-S batteries. *ACS Nano* **2020**, *14*, 8495–8507. [[CrossRef](#)] [[PubMed](#)]
26. Tang, T.; Zhang, T.; Zhao, L.; Zhang, B.; Li, W.; Xu, J.; Li, T.; Zhang, L.; Qiu, H.; Hou, Y. Multifunctional V<sub>3</sub>S<sub>4</sub>-nanowire/graphene composites for high performance Li-S batteries. *Sci. China Mater.* **2020**, *63*, 1910–1919. [[CrossRef](#)]
27. Pang, Q.; Liang, X.; Kwok, C.Y.; Nazar, L.F. Advances in lithium-sulfur batteries based on multifunctional cathodes and electrolytes. *Nat. Energy* **2016**, *1*, 16132. [[CrossRef](#)]

28. Yang, A.; Zhou, G.; Kong, X.; Vilá, R.A.; Pei, A.; Wu, Y.; Yu, X.; Zheng, X.; Wu, C.; Liu, B.; et al. Electrochemical generation of liquid and solid sulfur on two-dimensional layered materials with distinct areal capacities. *Nat. Nanotechnol.* **2020**, *15*, 231–237. [[CrossRef](#)]
29. Xiao, F.; Yang, X.; Yao, T.; Wang, H.; Rogach, A.L. Encapsulation of selenium in MOF-derived N,O-codoped porous flower-like carbon host for Na-Se batteries. *Chem. Eng. J.* **2022**, *430*, 132737. [[CrossRef](#)]
30. Li, Y.; Wang, M.; Chen, Y.; Hu, L.; Liu, T.; Bao, S.; Xu, M. Muscle-like electrode design for Li-Te batteries. *Energy Storage Mater.* **2018**, *10*, 10–15. [[CrossRef](#)]
31. Zhao, Z.; Chen, W.; Impeng, S.; Li, M.; Wang, R.; Liu, Y.; Zhang, L.; Dong, L.; Unruangsri, J.; Peng, C.; et al. Covalent organic framework-based ultrathin crystalline porous film: Manipulating uniformity of fluoride distribution for stabilizing lithium metal anode. *J. Mater. Chem. A* **2020**, *8*, 3459–3467. [[CrossRef](#)]
32. Li, Y.; Li, Y.; Pei, A.; Yan, K.; Sun, Y.; Wu, C.L.; Joubert, L.M.; Chin, R.; Koh, A.L.; Yu, Y.; et al. Atomic structure of sensitive battery materials and interfaces revealed by cryo-electron microscopy. *Science* **2017**, *358*, 506–510. [[CrossRef](#)] [[PubMed](#)]
33. Qin, J.; Shi, H.; Huang, K.; Lu, P.; Wen, P.; Xing, F.; Yang, B.; Ye, M.; Yu, Y.; Wu, Z. Achieving stable Na metal cycling via polydopamine/multilayer graphene coating of a polypropylene separator. *Nat. Commun.* **2021**, *12*, 5786. [[CrossRef](#)] [[PubMed](#)]
34. Tang, X.; Zhou, D.; Li, P.; Guo, X.; Sun, B.; Liu, H.; Yan, K.; Gogotsi, Y.; Wang, G. MXene-based dendrite-free potassium metal batteries. *Adv. Mater.* **2020**, *32*, 1906739. [[CrossRef](#)]
35. Liu, J.; Zhou, W.; Zhao, R.; Yang, Z.; Li, W.; Chao, D.; Qiao, S.; Zhao, D. Sulfur-based aqueous batteries: Electrochemistry and strategies. *J. Am. Chem. Soc.* **2021**, *143*, 15475–15489. [[CrossRef](#)]
36. Chao, D.; Zhou, W.; Xie, F.; Ye, C.; Li, H.; Jaroniec, M.; Qiao, S.Z. Roadmap for advanced aqueous batteries: From design of materials to applications. *Sci Adv.* **2020**, *6*, a4098. [[CrossRef](#)] [[PubMed](#)]
37. Cai, S.Y.; Chu, X.Y.; Liu, C.; Lai, H.W.; Chen, H.; Jiang, Y.Q.; Guo, F.; Xu, Z.K.; Wang, C.S.; Gao, C. Water-salt oligomers enable supersoluble electrolytes for high-performance aqueous batteries. *Adv. Mater.* **2021**, *33*, 2007470. [[CrossRef](#)]
38. Zhang, T.; Chen, Q.; Li, X.; Liu, J.; Zhou, W.; Wang, B.; Zhao, Z.; Li, W.; Chao, D.; Zhao, D. Redox mediator chemistry regulated aqueous batteries: Insights into mechanisms and prospects. *CCS Chem.* **2022**, *4*, 2874–2887. [[CrossRef](#)]
39. Chao, D.; Qiao, S. Toward high-voltage aqueous batteries: Super- or low-concentrated electrolyte? *Joule* **2020**, *4*, 1846–1851. [[CrossRef](#)]
40. Chen, G.; Sang, Z.; Cheng, J.; Tan, S.; Yi, Z.; Zhang, X.; Si, W.; Yin, Y.; Liang, J.; Hou, F. Reversible and homogenous zinc deposition enabled by in-situ grown Cu particles on expanded graphite for dendrite-free and flexible zinc metal anodes. *Energy Storage Mater.* **2022**, *50*, 589–597. [[CrossRef](#)]
41. Cao, Q.; Gao, H.; Gao, Y.; Yang, J.; Li, C.; Pu, J.; Du, J.; Yang, J.; Cai, D.; Pan, Z.; et al. Regulating dendrite-free zinc deposition by 3D zincophilic nitrogen-doped vertical graphene for high-performance flexible Zn-ion batteries. *Adv. Funct. Mater.* **2021**, *31*, 2103922. [[CrossRef](#)]
42. Lv, Y.; Xiao, Y.; Ma, L.; Zhi, C.; Chen, S. Recent advances in electrolytes for “beyond aqueous” zinc-ion batteries. *Adv. Mater.* **2022**, *34*, 2106409. [[CrossRef](#)] [[PubMed](#)]
43. Li, G.; Liu, Z.; Huang, Q.; Gao, Y.; Regula, M.; Wang, D.; Chen, L.; Wang, D. Stable metal battery anodes enabled by polyethylenimine sponge hosts by way of electrokinetic effects. *Nat. Energy* **2018**, *3*, 1076–1083. [[CrossRef](#)]
44. Ma, L.; Schroeder, M.A.; Borodin, O.; Pollard, T.P.; Ding, M.S.; Wang, C.; Xu, K. Realizing high zinc reversibility in rechargeable batteries. *Nat. Energy* **2020**, *5*, 743–749. [[CrossRef](#)]
45. Parker, J.F.; Chervin, C.N.; Pala, I.R.; Machler, M.; Burz, M.F.; Long, J.W.; Rolison, D.R. Rechargeable nickel-3D zinc batteries: An energy-dense, safer alternative to lithium-ion. *Science* **2017**, *356*, 414–417. [[CrossRef](#)] [[PubMed](#)]
46. Zhou, J.; Wu, F.; Mei, Y.; Hao, Y.; Li, L.; Xie, M.; Chen, R. Establishing thermal infusion method for stable zinc metal anodes in aqueous zinc-ion batteries. *Adv. Mater.* **2022**, *34*, 2200782. [[CrossRef](#)]
47. Xiong, L.; Fu, H.; Han, W.; Wang, M.; Li, J.; Yang, W.; Liu, G. Robust ZnS interphase for stable Zn metal anode of high-performance aqueous secondary batteries. *Int. J. Miner. Metall. Mater.* **2022**, *29*, 1053–1060. [[CrossRef](#)]
48. Li, H.; Guo, C.; Zhang, T.; Xue, P.; Zhao, R.; Zhou, W.; Li, W.; Elzatahry, A.; Zhao, D.; Chao, D. Hierarchical confinement effect with zincophilic and spatial traps stabilized Zn-based aqueous battery. *Nano Lett.* **2022**, *22*, 4223–4231. [[CrossRef](#)]
49. Chen, X.; Ruan, P.; Wu, X.; Liang, S.; Zhou, J. Crystal structures, reaction mechanisms, and optimization strategies of MnO<sub>2</sub> cathode for aqueous rechargeable zinc batteries. *Acta Phys. Chim. Sin.* **2022**, *38*, 2111003.
50. Song, Y.; Ruan, P.; Mao, C.; Chang, Y.; Wang, L.; Dai, L.; Zhou, P.; Lu, B.; Zhou, J.; He, Z. Metal-organic frameworks functionalized separators for robust aqueous zinc-ion batteries. *Nano-Micro Lett.* **2022**, *14*, 218. [[CrossRef](#)]
51. Pan, H.; Shao, Y.; Yan, P.; Cheng, Y.; Han, K.S.; Nie, Z.; Wang, C.; Yang, J.; Li, X.; Bhattacharya, P.; et al. Reversible aqueous zinc/manganese oxide energy storage from conversion reactions. *Nat. Energy* **2016**, *1*, 16039. [[CrossRef](#)]
52. Zhang, L.; Hou, Y. Comprehensive analyses of aqueous Zn metal batteries: Characterization methods, simulations, and theoretical calculations. *Adv. Energy Mater.* **2021**, *11*, 2003823. [[CrossRef](#)]
53. Canepa, P.; Sai Gautam, G.; Hannah, D.C.; Malik, R.; Liu, M.; Gallagher, K.G.; Persson, K.A.; Ceder, G. Odyssey of multivalent cathode materials: Open questions and future challenges. *Chem. Rev.* **2017**, *117*, 4287–4341. [[CrossRef](#)]
54. Zhu, K.; Wei, S.; Shou, H.; Shen, F.; Chen, S.; Zhang, P.; Wang, C.; Cao, Y.; Guo, X.; Luo, M.; et al. Defect engineering on V<sub>2</sub>O<sub>3</sub> cathode for long-cycling aqueous zinc metal batteries. *Nat. Commun.* **2021**, *12*, 6878. [[CrossRef](#)]

55. Lee, W.S.V.; Xiong, T.; Wang, X.; Xue, J. Unraveling MoS<sub>2</sub> and transition metal dichalcogenides as functional zinc-ion battery cathode: A perspective. *Small Methods* **2021**, *5*, 2000815. [[CrossRef](#)]
56. Kundu, D.; Oberholzer, P.; Glaros, C.; Bouzid, A.; Tervoort, E.; Pasquarello, A.; Niederberger, M. Organic cathode for aqueous Zn-ion batteries: Taming a unique phase evolution toward stable electrochemical cycling. *Chem. Mater.* **2018**, *30*, 3874–3881. [[CrossRef](#)]
57. Yong, B.; Ma, D.; Wang, Y.; Mi, H.; He, C.; Zhang, P. Understanding the design principles of advanced aqueous zinc-ion battery cathodes: From transport kinetics to structural engineering, and future perspectives. *Adv. Energy Mater.* **2020**, *10*, 2002354. [[CrossRef](#)]
58. Pam, M.E.; Yan, D.; Yu, J.; Fang, D.; Guo, L.; Li, X.L.; Li, T.C.; Lu, X.; Ang, L.K.; Amal, R.; et al. Microstructural engineering of cathode materials for advanced zinc-ion aqueous batteries. *Adv. Sci.* **2021**, *8*, 2002722. [[CrossRef](#)]
59. Sun, Y.; Xu, Z.; Xu, X.; Nie, Y.; Tu, J.; Zhou, A.; Zhang, J.; Qiu, L.; Chen, F.; Xie, J.; et al. Low-cost and long-life Zn/Prussian blue battery using a water-in-ethanol electrolyte with a normal salt concentration. *Energy Storage Mater.* **2022**, *48*, 192–204. [[CrossRef](#)]
60. Yang, K.; Hu, Y.; Zhang, T.; Wang, B.; Qin, J.; Li, N.; Zhao, Z.; Zhao, J.; Chao, D. Triple-functional polyoxovanadate cluster in regulating cathode, anode, and electrolyte for tough aqueous zinc-ion battery. *Adv. Energy Mater.* **2022**, *12*, 2202671. [[CrossRef](#)]
61. Zhang, H.; Shang, Z.; Luo, G.; Jiao, S.; Cao, R.; Chen, Q.; Lu, K. Redox catalysis promoted activation of sulfur redox chemistry for energy-dense flexible solid-state Zn-S Battery. *ACS Nano* **2022**, *16*, 7344–7351. [[CrossRef](#)] [[PubMed](#)]
62. Dai, C.; Jin, X.; Ma, H.; Hu, L.; Sun, G.; Chen, H.; Yang, Q.; Xu, M.; Liu, Q.; Xiao, Y.; et al. Maximizing energy storage of flexible aqueous batteries through decoupling charge carriers. *Adv. Energy Mater.* **2021**, *11*, 2003982. [[CrossRef](#)]
63. Zhou, T.; Wan, H.; Liu, M.; Wu, Q.; Fan, Z.; Zhu, Y. Regulating uniform nucleation of ZnS enables low-polarized and high stable aqueous Zn-S batteries. *Mater. Today Energy* **2022**, *27*, 101025. [[CrossRef](#)]
64. Xu, Z.; Zhang, Y.; Gou, W.; Liu, M.; Sun, Y.; Han, X.; Sun, W.; Li, C. The key role of concentrated Zn(OTF)<sub>2</sub> electrolyte in the performance of aqueous Zn-S batteries. *Chem. Commun.* **2022**, *58*, 8145–8148. [[CrossRef](#)] [[PubMed](#)]
65. Chen, Z.; Mo, F.N.; Wang, T.R.; Yang, Q.; Huang, Z.D.; Wang, D.H.; Liang, G.J.; Chen, A.; Li, Q.; Guo, Y.; et al. Zinc/selenium conversion battery: A system highly compatible with both organic and aqueous electrolytes. *Energy Environ. Sci.* **2021**, *14*, 2441–2450. [[CrossRef](#)]
66. Chen, Z.; Yang, Q.; Mo, F.; Li, N.; Liang, G.; Li, X.; Huang, Z.; Wang, D.; Huang, W.; Fan, J.; et al. Aqueous zinc-tellurium batteries with ultraflat discharge plateau and high volumetric capacity. *Adv. Mater.* **2020**, *32*, 2001469. [[CrossRef](#)]
67. Wu, X.; Markir, A.; Ma, L.; Xu, Y.; Jiang, H.; Leonard, D.P.; Shin, W.; Wu, T.; Lu, J.; Ji, X. A four-electron sulfur electrode hosting a Cu<sup>2+</sup>/Cu<sup>+</sup> redox charge carrier. *Angew. Chem. Int. Ed.* **2019**, *58*, 12640–12645. [[CrossRef](#)]
68. Dai, C.; Hu, L.; Chen, H.; Jin, X.; Han, Y.; Wang, Y.; Li, X.; Zhang, X.; Song, L.; Xu, M.; et al. Enabling fast-charging selenium-based aqueous batteries via conversion reaction with copper ions. *Nat. Commun.* **2022**, *13*, 1863. [[CrossRef](#)]
69. Chen, Z.; Cui, H.; Hou, Y.; Wang, X.; Jin, X.; Chen, A.; Yang, Q.; Wang, D.; Huang, Z.; Zhi, C. Anion chemistry enabled positive valence conversion to achieve a record high-voltage organic cathode for zinc batteries. *Chem* **2022**, *8*, 2204–2216. [[CrossRef](#)]
70. Yu, B.; Huang, A.; Srinivas, K.; Zhang, X.; Ma, F.; Wang, X.; Chen, D.; Wang, B.; Zhang, W.; Wang, Z.; et al. Outstanding catalytic effects of 1T'-MoTe<sub>2</sub> quantum dots@3D graphene in shuttle-free Li-S batteries. *ACS Nano* **2021**, *15*, 13279–13288. [[CrossRef](#)]
71. Wang, H.; Jamil, S.; Tang, W.; Zhao, J.; Liu, H.; Bao, S.; Liu, Y.; Xu, M. Melamine-sacrificed pyrolytic synthesis of spiderweb-like nanocages encapsulated with catalytic Co atoms as cathode for advanced Li-S batteries. *Batteries* **2022**, *8*, 161. [[CrossRef](#)]
72. Kang, N.; Lin, Y.; Yang, L.; Lu, D.; Xiao, J.; Qi, Y.; Cai, M. Cathode porosity is a missing key parameter to optimize lithium-sulfur battery energy density. *Nat. Commun.* **2019**, *10*, 4597. [[CrossRef](#)]
73. Yang, M.; Yan, Z.; Xiao, J.; Xin, W.; Zhang, L.; Peng, H.; Geng, Y.; Li, J.; Wang, Y.; Liu, L.; et al. Boosting cathode activity and anode stability of Zn-S batteries in aqueous media through cosolvent-catalyst synergy. *Angew. Chem. Int. Ed.* **2022**, *61*, e202212666.
74. Li, W.; Wang, K.; Jiang, K. A Low cost aqueous Zn-S battery realizing ultrahigh energy density. *Adv. Sci.* **2020**, *7*, 2000761. [[CrossRef](#)]
75. Wang, F.; Borodin, O.; Gao, T.; Fan, X.; Sun, W.; Han, F.; Faraone, A.; Dura, J.A.; Xu, K.; Wang, C. Highly reversible zinc metal anode for aqueous batteries. *Nat. Mater.* **2018**, *17*, 543–549. [[CrossRef](#)]
76. Zhang, L.; Zhang, B.; Zhang, T.; Li, T.; Shi, T.; Li, W.; Shen, T.; Huang, X.; Xu, J.; Zhang, X.; et al. Eliminating dendrites and side reactions via a multifunctional ZnSe protective layer toward advanced aqueous Zn metal batteries. *Adv. Funct. Mater.* **2021**, *31*, 2100186. [[CrossRef](#)]
77. Zhang, W.; Dong, M.; Jiang, K.; Yang, D.; Tan, X.; Zhai, S.; Feng, R.; Chen, N.; King, G.; Zhang, H.; et al. Self-repairing interphase reconstructed in each cycle for highly reversible aqueous zinc batteries. *Nat. Commun.* **2022**, *13*, 5348. [[CrossRef](#)]
78. Zhao, Z.; Wang, R.; Peng, C.; Chen, W.; Wu, T.; Hu, B.; Weng, W.; Yao, Y.; Zeng, J.; Chen, Z.; et al. Horizontally arranged zinc platelet electrode deposits modulated by fluorinated covalent organic framework film for high-rate and durable aqueous zinc ion batteries. *Nat. Commun.* **2021**, *12*, 6606. [[CrossRef](#)]
79. Xie, F.; Li, H.; Wang, X.; Zhi, X.; Chao, D.; Davey, K.; Qiao, S.Z. Mechanism for zincophilic sites on zinc-metal anode hosts in aqueous batteries. *Adv. Energy Mater.* **2021**, *11*, 2003419. [[CrossRef](#)]
80. Luo, L.; Zhang, C.; Wu, X.; Han, C.; Xu, Y.; Ji, X.; Jiang, J. A Zn-S aqueous primary battery with high energy and flat discharge plateau. *Chem. Commun.* **2021**, *57*, 9918–9921. [[CrossRef](#)]

81. Wang, C.; Pei, Z.; Meng, Q.; Zhang, C.; Sui, X.; Yuan, Z.; Wang, S.; Chen, Y. Toward flexible zinc-ion hybrid capacitors with superhigh energy density and ultralong cycling life: The pivotal role of  $\text{ZnCl}_2$  salt-based electrolytes. *Angew. Chem. Int. Ed.* **2021**, *60*, 990–997. [[CrossRef](#)]
82. Zhang, N.; Cheng, F.; Liu, Y.; Zhao, Q.; Lei, K.; Chen, C.; Liu, X.; Chen, J. Cation-deficient spinel  $\text{ZnMn}_2\text{O}_4$  cathode in  $\text{Zn}(\text{CF}_3\text{SO}_3)_2$  electrolyte for rechargeable aqueous Zn-ion battery. *J. Am. Chem. Soc.* **2016**, *138*, 12894–12901. [[CrossRef](#)] [[PubMed](#)]
83. Cui, M.; Fei, J.; Mo, F.; Lei, H.; Huang, Y. Ultra-high-capacity and dendrite-free zinc-sulfur conversion batteries based on a low-cost deep eutectic solvent. *ACS Appl. Mater. Interfaces* **2021**, *13*, 54981–54989. [[CrossRef](#)] [[PubMed](#)]
84. Dai, C.; Hu, L.; Jin, X.; Chen, H.; Zhang, X.; Zhang, S.; Song, L.; Ma, H.; Xu, M.; Zhao, Y.; et al. A cascade battery: Coupling two sequential electrochemical reactions in a single battery. *Adv. Mater.* **2021**, *33*, 2105480. [[CrossRef](#)] [[PubMed](#)]
85. Guo, Z.; Li, C.; Liu, J.; Wang, Y.; Xia, Y. A long-life lithium-air battery in ambient air with a polymer electrolyte containing a redox mediator. *Angew. Chem. Int. Ed.* **2017**, *56*, 7505–7509. [[CrossRef](#)] [[PubMed](#)]
86. Tułodziecki, M.; Leverick, G.M.; Amanchukwu, C.V.; Katayama, Y.; Kwabi, D.G.; Bardé, F.; Hammond, P.T.; Shao-Horn, Y. The role of iodide in the formation of lithium hydroxide in lithium-oxygen batteries. *Energy Environ. Sci.* **2017**, *10*, 1828–1842. [[CrossRef](#)]
87. Yang, H.; Qiao, Y.; Chang, Z.; Deng, H.; He, P.; Zhou, H. A metal-organic framework as a multifunctional ionic sieve membrane for long-life aqueous zinc-iodide batteries. *Adv. Mater.* **2020**, *32*, 2004240. [[CrossRef](#)]
88. Zhang, S.J.; Hao, J.; Li, H.; Zhang, P.F.; Yin, Z.W.; Li, Y.Y.; Zhang, B.; Lin, Z.; Qiao, S.Z. Polyiodide confinement by starch enables shuttle-free Zn-iodine batteries. *Adv. Mater.* **2022**, *34*, 2201716. [[CrossRef](#)]
89. Zhao, Y.; Wang, D.; Li, X.; Yang, Q.; Guo, Y.; Mo, F.; Li, Q.; Peng, C.; Li, H.; Zhi, C. Initiating a reversible aqueous Zn/sulfur battery through a “liquid film”. *Adv. Mater.* **2020**, *32*, 2003070. [[CrossRef](#)]
90. Liu, D.; He, B.; Zhong, Y.; Chen, J.; Yuan, L.; Li, Z.; Huang, Y. A durable ZnS cathode for aqueous Zn-S batteries. *Nano Energy* **2022**, *101*, 107474. [[CrossRef](#)]
91. Gu, X.; Xin, L.; Li, Y.; Dong, F.; Fu, M.; Hou, Y. Highly reversible Li-Se batteries with ultra-lightweight N,S-codoped graphene blocking layer. *Nano-Micro Lett.* **2018**, *10*, 59. [[CrossRef](#)]
92. Mukkabl, R.; Deshagani, S.; Meduri, P.; Deepa, M.; Ghosal, P. Selenium/graphite platelet nanofiber composite for durable Li–Se batteries. *ACS Energy Lett.* **2017**, *2*, 1288–1295. [[CrossRef](#)]
93. Wang, H.; Lai, K.; Guo, F.; Long, B.; Zeng, X.; Fu, Z.; Wu, X.; Xiao, Y.; Dou, S.; Dai, J. Theoretical calculation guided materials design and capture mechanism for Zn–Se batteries via heteroatom-doped carbon. *Carbon Neutralization* **2022**, *1*, 59–67. [[CrossRef](#)]
94. Dong, W.; Chen, H.; Xia, F.; Yu, W.; Song, J.; Wu, S.; Deng, Z.; Hu, Z.; Hasan, T.; Li, Y.; et al. Selenium clusters in Zn-glutamate MOF derived nitrogen-doped hierarchically radial-structured microporous carbon for advanced rechargeable Na-Se batteries. *J. Mater. Chem. A* **2018**, *6*, 22790–22797. [[CrossRef](#)]
95. Song, J.; Wu, L.; Dong, W.; Li, C.; Chen, L.; Dai, X.; Li, C.; Chen, H.; Zou, W.; Yu, W.; et al. MOF-derived nitrogen-doped core-shell hierarchical porous carbon confining selenium for advanced lithium-selenium batteries. *Nanoscale* **2019**, *11*, 6970–6981. [[CrossRef](#)]
96. Du, Y.; Ma, S.; Dai, J.; Lin, J.; Zhou, X.; Chen, T.; Gu, X. Biomass carbon materials contribute better alkali-metal-selenium batteries: A mini-review. *Batteries* **2022**, *8*, 123. [[CrossRef](#)]
97. Ma, L.; Ying, Y.; Chen, S.; Chen, Z.; Li, H.; Huang, H.; Zhao, L.; Zhi, C. Electrocatalytic selenium redox reaction for high-mass-loading zinc-selenium batteries with improved kinetics and selenium utilization. *Adv. Energy Mater.* **2022**, *12*, 2201322. [[CrossRef](#)]
98. Li, W.; Ma, Y.; Li, P.; Jing, X.; Jiang, K.; Wang, D. Synergistic effect between S and Se enhancing the electrochemical behavior of  $\text{Se}_x\text{S}_y$  in aqueous Zn metal batteries. *Adv. Funct. Mater.* **2021**, *31*, 2101237. [[CrossRef](#)]
99. Chen, Z.; Yang, Q.; Wang, D.; Chen, A.; Li, X.; Huang, Z.; Liang, G.; Wang, Y.; Zhi, C. Tellurium: A high-performance cathode for magnesium ion batteries based on a conversion mechanism. *ACS Nano* **2022**, *16*, 5349–5357. [[CrossRef](#)]
100. Chen, Z.; Zhao, Y.; Mo, F.; Huang, Z.; Li, X.; Wang, D.; Liang, G.; Yang, Q.; Chen, A.; Li, Q.; et al. Metal-tellurium batteries: A rising energy storage system. *Small Struct.* **2020**, *1*, 2000005. [[CrossRef](#)]
101. Dong, S.; Yu, D.D.; Yang, J.; Jiang, L.; Wang, J.W.; Cheng, L.W.; Zhou, Y.; Yue, H.L.; Wang, H.; Guo, L. Tellurium: A high-volumetric-capacity potassium-ion battery electrode material. *Adv. Mater.* **2020**, *32*, 1908027. [[CrossRef](#)] [[PubMed](#)]
102. Zhang, Y.; Lu, W.; Zhao, P.; Aboonassr Shiraz, M.H.; Manaig, D.; Freschi, D.J.; Liu, Y.; Liu, J. A durable lithium-tellurium battery: Effects of carbon pore structure and tellurium content. *Carbon* **2021**, *173*, 11–21. [[CrossRef](#)]
103. Liu, Y.; Wang, J.; Xu, Y.; Zhu, Y.; Bigio, D.; Wang, C. Lithium-tellurium batteries based on tellurium/porous carbon composite. *J. Mater. Chem. A* **2014**, *2*, 12201–12207. [[CrossRef](#)]
104. Wang, J.; Du, J.; Zhao, J.; Wang, Y.; Tang, Y.; Cui, G. Unraveling  $\text{H}^+/\text{Zn}^{2+}$  sequential conversion reactions in tellurium cathodes for rechargeable aqueous zinc batteries. *J. Phys. Chem. Lett.* **2021**, *12*, 10163–10168. [[CrossRef](#)]
105. Wang, J.; Yang, Y.; Wang, Y.; Dong, S.; Cheng, L.; Li, Y.; Wang, Z.; Trabzon, L.; Wang, H. Working aqueous Zn metal batteries at 100 °C. *ACS Nano* **2022**, *16*, 15770–15778. [[CrossRef](#)] [[PubMed](#)]
106. Xie, J.; Liang, Z.; Lu, Y. Molecular crowding electrolytes for high-voltage aqueous batteries. *Nat. Mater.* **2020**, *19*, 1006–1011. [[CrossRef](#)] [[PubMed](#)]
107. Park, M.J.; Yaghoobnejad Asl, H.; Manthiram, A. multivalent-ion versus proton insertion into battery electrodes. *ACS Energy Lett.* **2020**, *5*, 2367–2375. [[CrossRef](#)]
108. Ghosh, M.; Vijayakumar, V.; Kurian, M.; Dilwale, S.; Kurungot, S. Naphthalene dianhydride organic anode for a ‘rocking-chair’ zinc-proton hybrid ion battery. *Dalton Trans.* **2021**, *50*, 4237–4243. [[CrossRef](#)]

109. Peng, L.; Ren, X.; Liang, Z.; Sun, Y.; Zhao, Y.; Zhang, J.; Yao, Z.; Ren, Z.; Li, Z.; Wang, J.; et al. Reversible proton co-intercalation boosting zinc-ion adsorption and migration abilities in bismuth selenide nanoplates for advanced aqueous batteries. *Energy Storage Mater.* **2021**, *42*, 34–41. [[CrossRef](#)]
110. Li, M.; Zhang, Y.; Hu, J.; Wang, X.; Zhu, J.; Niu, C.; Han, C.; Mai, L. Universal multifunctional hydrogen bond network construction strategy for enhanced aqueous Zn<sup>2+</sup>/proton hybrid batteries. *Nano Energy* **2022**, *100*, 107539. [[CrossRef](#)]

**Disclaimer/Publisher's Note:** The statements, opinions and data contained in all publications are solely those of the individual author(s) and contributor(s) and not of MDPI and/or the editor(s). MDPI and/or the editor(s) disclaim responsibility for any injury to people or property resulting from any ideas, methods, instructions or products referred to in the content.